The Astrophysical Journal Supplement Series, 208:10 (26pp), 2013 September doi:10.1088/0067-0049/208/1/10

NEW STRONG-LINE ABUNDANCE DIAGNOSTICS FOR H II REGIONS: EFFECTS OF κ-DISTRIBUTED ELECTRON ENERGIES AND NEW ATOMIC DATA

Michael A. Dopita[1,2,3], Ralph S. Sutherland[1], David C. Nicholls[1], Lisa J. Kewley[1,3], and Frédéric P. A. Vogt[1]
[1] Research School of Astronomy and Astrophysics, Australian National University, Cotter Rd., Weston ACT 2611, Australia; Michael.Dopita@anu.edu.au
[2] Astronomy Department, King Abdulaziz University, P.O. Box 80203, Jeddah, Saudi Arabia
[3] Institute for Astronomy, University of Hawaii, 2680, Woodlawn Drive, Honolulu, HI 96822, USA
Received 2013 April 7; accepted 2013 July 15; published 2013 September 4

ABSTRACT

Recently, Nicholls et al., inspired by in situ observations of solar system astrophysical plasmas, suggested that the electrons in H II regions are characterized by a κ-distribution of energies rather than a simple Maxwell–Boltzmann distribution. Here, we have collected together new atomic data within a modified photoionization code to explore the effects of both the new atomic data and the κ-distribution on the strong-line techniques used to determine chemical abundances in H II regions. By comparing the recombination temperatures ($T_{\rm rec}$) with the forbidden line temperatures ($T_{\rm FL}$), we conclude that $\kappa \sim 20$. While representing only a mild deviation from equilibrium, this result is sufficient to strongly influence abundances determined using methods that depend on measurements of the electron temperature from forbidden lines. We present a number of new emission line ratio diagnostics that cleanly separate the two parameters determining the optical spectrum of H II regions—the ionization parameter q or $\mathcal{U}$ and the chemical abundance, 12+log(O/H). An automated code to extract these parameters is presented. Using the homogeneous data set from van Zee et al., we find self-consistent results between all of these different diagnostics. The systematic errors between different line ratio diagnostics are much smaller than those found in the earlier strong-line work. Overall, the effect of the κ-distribution on the strong-line abundances derived solely on the basis of theoretical models is rather small.

Key words: atomic data – atomic processes – H II regions – ISM: abundances – plasmas

Online-only material: color figures, machine-readable tables

1. INTRODUCTION

Much of what we know—or believe we understand—about the chemical evolution history of the universe depends upon the interpretation of the strong emission lines originating from H II regions in distant galaxies. These emission lines enable us to investigate the metallicity evolution of the universe as a whole (Nagamine et al. 2001; De Lucia et al. 2004; Kobayashi et al. 2007; Yuan et al. 2013). We may also measure the mass–metallicity relationship of disk galaxies (see Kewley & Ellison 2008 and references therein), understand how chemical abundance gradients are formed and maintained (Bothun et al. 1984; Wyse & Silk 1985; Skillman et al. 1989; Vila-Costas & Edmunds 1992; Zaritsky et al. 1994; van Zee et al. 1998), and discover how abundance gradients can be removed in galaxy interactions (Kewley et al. 2010; Rupke et al. 2010; Torrey et al. 2012; Rich et al. 2012). Chemical abundances also encode information about the history of star formation, mass infall, and radial mixing driven by viscous processes in galactic disks.

The "classical" technique to derive chemical abundances first uses the observed temperature, T_e, derived from temperature sensitive line ratios such as [O III] λ4363/[O III] λ5007 in combination with the ratio of a strong forbidden line of the element of interest to a Balmer line of hydrogen to estimate the abundance of the observed ion of a given atomic species. For those ions that do not produce an observable line in the optical, we estimate an ionization correction factor (ICF) based upon theory to account for the abundance of the unobserved ions of the same atomic species. This T_e + ICF technique has been very extensively used over the past 50 yr since it was first devised by Aller & Liller (1959) and further developed by Peimbert (1967) and Peimbert & Costero (1969).

Later on, strong line techniques were developed that simply relied on the ratio of forbidden lines to the hydrogen recombination lines, a natural enough approach if we believe that such ratios encode information about the relative abundance of the ion considered compared to hydrogen. The most commonly used ratios are often referred to by their shorthand contractions: R_2 = [O II] $\lambda\lambda$3726, 9/Hβ, R_3 = [O III] λ5007/Hβ, $R_{23} = R_2 + R_3$ (Pagel et al. 1979), and similar ratios involving S, for example S_{23} = ([S II] $\lambda\lambda$6717, 31 + [S III] $\lambda\lambda$9069, 9532)/Hβ (Diaz & Pérez-Montero 2000; Oey et al. 2002). The abundance calibration for these ratios may either be based purely on photoionization models, or on an empirical calibration based upon alignment of the abundance scale to objects for which the T_e+ ICF technique has been used. Strong-line techniques that depend on ratios involving hydrogen recombination lines suffer from a fundamental ambiguity, in that these line ratios decreases at both the low- and high-abundance ends, requiring some other technique to resolve in which "branch" the observed H II region lies.

Despite the best efforts of theoreticians, the degree of scatter among the different strong emission line diagnostics remains alarming (e.g., Kewley & Dopita 2002; Kewley & Ellison 2008; López-Sánchez et al. 2012) and this scatter is strongly dependent on the approach used to estimate abundances from such ratios. Some approaches rely entirely on the construction of theoretical H II region models using stellar model atmospheres and photoionization codes (McGaugh 1991; Dopita et al. 2000), while others seek to calibrate R_{23} or S_{23} in terms of the abundances derived from objects for which there are direct measurements of the electron temperature T_e from temperature sensitive line ratios such as [O III] λ4363/[O III] λ5007. This method was pioneered by Pagel et al. (1979) and Alloin

et al. (1979). This approach was used by Diaz & Pérez-Montero (2000), and has been investigated in great detail in a series of papers by Pilyugin and his collaborators (Pilyugin & Thuan 2005; Pilyugin & Mattsson 2011), culminating in the "counterpart" method of Pilyugin et al. (2012). A slightly different approach was used by van Zee et al. (1998), who computed the oxygen abundances with the McGaugh (1991) method, using the N II line to distinguish between the high- and low-abundance branches. van Zee et al. (1998) used this method to propose a calibration of N II/Hα. This technique is especially useful in the "turnover region" between the high- and low-abundance branches.

In addition to the uncertainties depending on whether a given H II region lies on the high- or low-abundance branch, and those associated with the theoretical or observational calibrations, considerable uncertainty is introduced into the derived strong line abundances in those cases where the ionization parameter is not explicitly solved for as a separate variable (Pagel et al. 1979; Alloin et al. 1979; Zaritsky et al. 1994; Pettini & Pagel 2004). The first authors to properly account for the effect of the ionization parameter were Evans & Dopita (1985, 1986), followed by McGaugh (1991). Although many bright H II regions are observed to have similar ionization parameters, the observed scatter in $\mathcal{U}$ or q introduces significant errors into the abundance estimates.

Even when all of these effects are accounted for, there remains a significant offset between those strong line techniques based purely upon photoionization models (McGaugh 1991; Kewley & Dopita 2002; Kobulnicky & Kewley 2004) and those based upon an empirical alignment of the strong line intensities to abundances derived in objects for which T_e has been directly estimated (Pilyugin 2001a, 2001b; Bresolin et al. 2004; Pilyugin & Thuan 2005; Pilyugin et al. 2012). The offset can be large, amounting to 0.3–0.5 dex, in the sense that the strong-line abundances estimated from a T_e abundance calibration are systematically lower than those estimated from models. This effect is clearly highlighted in López-Sánchez et al. (2012). The cause of this offset is the same as the systematic difference seen between abundances derived from model-based strong line techniques and those obtained by the traditional method of using the T_e+ ICF technique.

Three possibilities have been advanced to explain the offset in abundances between the strong line and the T_e+ ICF techniques:

1. The models predicting the strong lines do not deliver the correct electron temperature either because they do not consider all the necessary physics, or because the physical data they use are incorrect or incomplete.
2. Fluctuations or gradients in the electron temperature systematically bias the estimate of the temperature derived from line ratios such as [O III] λ4363/[O III] λ5007 (Peimbert & Costero 1969).
3. The measured electron temperature suffers from systematic errors relating to the choice of the input atomic data used to derive it. The size of such errors was recently quantified by Nicholls et al. (2013).

In order to eliminate the possibility that the strong line techniques have some systematic error, López-Sánchez et al. (2012) subjected a set of photoionization models from the MAPPINGS code (Sutherland & Dopita 1993; Allen et al. 2008) to a double-blind derivation of the abundances using the T_e + ICF technique. This experiment demonstrated that, for those species for which the optical line emission arises principally in the low-ionization zone of the H II region, N, S and Cl, the abundances input into the models could be recovered through the T_e + ICF analysis. However, for those species arising principally in the high-ionization zone of the H II region—O, Ne and Ar—a systematic shift of 0.2–0.3 dex is found. This result is in the same sense as the offset observed for real H II regions; the abundances estimated from a T_e + ICF calibration are systematically lower than those used in the photoionization models. Thus, at least part of the disagreement between the two techniques is due to real temperature gradients that exist in the high-ionization zones of the H II regions.

These large-scale temperature gradients play a role analogous to the small-scale temperature fluctuations proposed by Peimbert (1967) and used by very many others since then (e.g., Esteban 2002; García-Rojas & Esteban 2007; Peña-Guerrero et al. 2012). Kingdon & Ferland (1995) attempted to reproduce temperature fluctuations in the context of detailed photoionization models, and the whole thorny issue of their existence and theoretical justification was discussed by Stasińska (2004). Both temperature gradients and temperature fluctuations tend to increase the T_e estimated from the [O III] λ4363/[O III] λ5007 ratio, because the emissivity of the [O III] λ4363 line is biased toward the regions of higher T_e. This fact results in a systematic underestimate of the total chemical abundances. There are obvious physical causes for temperature gradients such as the hardening of the radiation field through radiative transfer effects and through the appearance or disappearance of important coolant ions, or through suppression of cooling by collisional de-excitation. Likewise, one can imagine physical causes of the small-scale temperature fluctuations (usually characterized by a parameter, t^2, the mean square fractional temperature fluctuation). These fluctuations could result from local turbulent heating or local shocks induced by colliding flows from ionization fronts. Such microphysics are not currently captured in photoionization codes.

Recently, Nicholls et al. (2012), inspired by in situ observations of astrophysical plasmas in and beyond the solar system, suggested that the electrons in H II regions may be characterized by a κ-distribution of energies rather than by a simple Maxwell–Boltzmann (M–B) distribution. Such distributions arise naturally in plasmas where there exist long-range energy transport processes (Livadiotis et al. 2011; Livadiotis & McComas 2011). These "hot tail" electron distributions can arise from plasma waves, magnetic re-connection, shocks, super-thermal atom or ion heating (as in a stellar wind H II region interaction zone), or by fast primary electrons produced by photoionization with X-ray or EUV photons. In many ways, the physical processes that may drive a microscopic κ-distribution of electrons are similar to those that may generate macroscopic temperature fluctuations, and neither can be discounted a priori.

Nicholls et al. (2012) demonstrated that a κ-distribution enhances the emissivity of the [O III] λ4363 line relative to [O III] λ5007, again resulting in a tendency for T_e to be systematically overestimated compared to the M–B distribution case. Similar considerations apply to other temperature-sensitive line ratios, as demonstrated by Nicholls et al. (2013). A cause for concern is that the newer fully-relativistic close-coupling calculations of atomic term energies and collision strengths such as those by Palay et al. (2012) provide a different absolute calibration from that used hitherto for these same temperature-sensitive ratios, as shown in Nicholls et al. (2013).

The three suggestions listed above suggest that there are grounds for supposing that abundances derived from either

strong-line techniques or from the T_e + ICF analysis may be in error. Likewise, the solution to the abundance discrepancy problem is likely to be found in a combination of one or more of these three effects, in addition to the temperature gradient issue already discussed above. We need to systematically take into account the newer atomic data and their effect on the photoionization models before we can investigate either the effect of the κ-distribution of electron energies in these photoionization models or how temperatures derived from line-sensitive line ratios are changed by use of either the new atomic data or by the application of a κ-distribution.

The purpose of the current paper is to provide the first systematic and quantitative study of the effect of the κ-distribution on the strong-line abundance diagnostics, not only at optical wavelengths, but also insofar as the strong UV and IR lines are concerned. The rest of the paper is organized as follows. In Section 2, we discuss what changes we have made to our photoionization code to incorporate both the new atomic data and the κ-distribution of electron energies. In Section 3, we explain the parameters of the photoionization models used in the grid of theoretical H II regions. In Section 4, we present a reference catalog of H II region models, varying the abundance set, the ionization parameter, and the value of κ. For each of the 324 models, we give the computed line intensities and a complete set of ionic and recombination temperatures. In Section 5, we estimate the likely value of κ using high-quality observations of Galactic and extragalactic H II regions. In Section 6, we discuss the effect of the κ-distribution on the intensities of the strong emission lines in both the UV and the far-IR regions of the spectrum. In Section 7, we present the results of the line ratio diagnostics and present a number of new line ratio diagrams that enable us to cleanly separate the effects of both the chemical abundance, 12+log(O/H), and the ionization parameter, q, from the strong-line spectra of H II regions. In Section 8, we compare the abundances derived for real data for H II regions using these diagnostic line ratios, and provide a code to derive for the plausible range of κ values, both the ionization parameter and abundance using the observed strong line ratios. Finally, we compare our derived abundances with earlier work on these same H II regions and provide a preliminary estimate of the effect that the κ-distribution has in producing a systematic offset between the strong-line and T_e + ICF techniques of deriving abundances.

2. THE MAPPINGS IV CODE

We have modified the MAPPINGS code (Sutherland & Dopita 1993; Allen et al. 2008) to incorporate new non-thermal (κ) electron energy excitation (Nicholls et al. 2012, 2013) and to bring the atomic data and the Maxwell-averaged collision strengths up to date. The number of ionic species treated as full non-local thermal equilibrium multi-level ions has increased from 37 to 43. The multi-level atoms are modeled using anywhere from three to nine levels depending on the ionic configuration. In particular—of particular relevance to H II region modeling—the species C I–C IV, N I–N V, O I–O VI, Ne III–Ne V, and S II–S IV are now uniformly handled. Ne II is still treated as a two-level atom for the purpose of computing its important 12.8 μm transition.

2.1. Energy Levels and Fundamental Constants

We have adopted the 2010 CODATA concordance on fundamental constants (Mohr et al. 2012). All multi-level atom energy level data are converted from derived energies in ergs to the more fundamental wavenumbers, in cm^{-1}. The cm^{-1} values were taken uniformly from the 2012 values in the NIST Atomic Spectroscopy Database v2 (Kramida et al. 2012) and are now independent of constants such as h or the value of the electron volt. While the effect of the change in the values of constants are small compared to the uncertainties in the level energies, when comparing values to boundary thresholds in the computation, more stable floating point representations now lead to a more stable execution of the code. The real benefit of this change is to reduce (although not eliminate) systematic differences in the treatment of different ionic species by adopting a more uniform set of atomic values, which was not readily possible in earlier decades.

2.2. Transition Probabilities

In addition to a uniform source of energy level data, recent advances in atomic structure calculations (Tachiev & Froese Fischer 1999, 2000, 2001, 2002) now suggest that the theoretical transition probabilities have become very accurate, even for forbidden M2 quadrupole transitions such as [O III] λ5006.8. In a study of the O III transitions, Froese Fischer et al. (2009) found excellent agreement at the level of 10% or better. With the advent of the NIST Multiconfiguration Hartree–Fock and Multiconfiguration Dirac–Hartree–Fock Database (MCHFD) now allows us to apply these transition probabilities uniformly for all the multi-level ions used in our models. This database, available at http://nlte.nist.gov/MCHF/, contains collections of transition data derived from different relativistic theories and by different computational methods.

2.3. Collision Strengths

For many of the multi-level atoms, the data used in MAPPINGS III (Sutherland & Dopita 1993; Allen et al. 2008) were merely translated to the new code format. However, for the important species, new electron energy-averaged collision strengths (Υ) were calculated from the original energy-resolved collision strength data (Ω) (either published or supplied as a private communication by the authors). The ions for which this treatment applies are listed in Nicholls et al. (2013). This approach enables two key features:

1. We can convolve the original Ω data with an M–B distribution to obtain energy-averaged collision strengths Υ values for any temperature and at any resolution desired, avoiding the interpolation errors that would arise if we depended only on published tabular data.
2. We are also able to convolve with κ non-thermal distributions and directly obtain the Υ_κ values.

In order to be able to rapidly evaluate both the M–B-averaged collision strength, Υ, and the equivalent κ-distribution-averaged collision strength, Υ_κ, we fit cubic spline functions in the following way:

1. High resolution integrals as a function of the Ω data convolved with the electron distributions were computed, $f(T)$, along with the local second derivative f'' at each point.
2. A fitting method akin to the one described in Press & Forbes (2007, p. 120 et seq.) was employed, except that we used the actual second derivative from the high-resolution integrals instead of a least squares fit to f at the subset of nodes.
3. By fixing the second derivative with the physical integral, the fitting procedure then became one of choosing the location of the spline nodes that minimized the difference

between the spline fit and the high-resolution integral data, evaluating the spline at the data points, usually 1000–3000 points. With optimal manual adjustment, the global error between the spline with 17 points and the high-resolution data was less than 0.001 and generally $\ll 5\times10^{-4}$ rms, achieving approximately third order accuracy, and better than that in some regions.

4. The temperature coordinates were normalized in a fashion similar to that used in CHIANTI 7.1 (Dere et al. 1997; Landi et al. 2012) and originally proposed by Burgess & Tully (1992), but here we use a more direct scaled temperature coordinate $x = T/(T+T_C)$, where T is the temperature and T_C is a characteristic temperature, chosen for each transition so that the main features of the Upsilon curve are well modeled. T_C is not directly related to the threshold energy, as used by Burgess & Tully (1992) and CHIANTI, but is related to structure in the Υ curve with energies characteristic of the major resonances in the underlying Ω data.

This transform has the property of scaling the temperature to $0 \leqslant x \leqslant 1$ and, by including spline nodes at or very near $x = 0$ and 1, ensures that the cubic spline interpolation is very stable at extreme temperature values when transformed back to a physical temperature scale, eliminating the well-known instability of cubic spline extrapolation. In the atomic data fitting procedure, every spline fit to every transition was plotted and evaluated.

2.4. Multi-level Atoms

The high resolution Maxwell-averaged collision strength data used in Nicholls et al. (2013) were adopted for O II (five levels), O III (six levels)), N II (six levels), S II (five levels), and S III (six levels). For Ne III, Ne IV, and Ne V, the spline fits given in CHIANTI 7.1 were transformed into the slightly different coordinate system used here. Lithium-like species, C IV (three levels), N V (three levels), and O VI (three levels) were fit from low-resolution tabular data given in the literature. Other important multi-level species include C I (five levels), C II (five levels), C III (five levels), N I (five levels), N III (five levels), N IV (four levels), O I (five levels), O IV (five levels). In the case of O V, S I, and S IV less detailed data were available, but we have nontheless included the temperature dependence. Table 1 lists all the sources of data we have used in this work.

2.5. Collisional Excitation Rates

The collisional excitation rate from energy level 1 to 2, R_{12}, depends on the collision strength $\Omega_{12}(E)$ and the energy E (cf. Nicholls et al. 2012):

$$R_{12} = n_e N_1 \frac{h^2}{8\pi m_e g_1} \int_{E_{12}}^{\infty} \frac{\Omega_{12}(E)}{\sqrt{E}}\, f(E) dE, \qquad (1)$$

where h is the Planck constant, m_e is the mass of the electron, g_1 is the statistical weight of the lower level, $f(E)$ is the energy distribution function, N_1 is the number density of atoms in the ground state, and n_e is is the electron density.

The collisional excitation rate from level 1 to level 2 for an M–B distribution is given by:

$$R_{12}(\mathrm{M-B}) = n_e N_1 \frac{h^2}{4\pi^{3/2} m_e g_1} (k_B T_U)^{-3/2} \times \int_{E_{12}}^{\infty} \Omega_{12}(E)\, \exp\left[-\frac{E}{k_B T_U}\right] dE. \qquad (2)$$

Table 1
Literature Sources Used for Collision Strength Data

Ion	Reference
C I	Pequignot & Aldrovandi (1976)
C II	Tayal (2008)
C III	Berrington et al. (1985)
C III	Berrington et al. (1989)
C IV	Liang & Badnell (2011)
N I	Tayal (2000)
N I	Tayal (2006)
N II	Tayal (2011)
N III	Stafford et al. (1994)
N IV	Ramsbottom et al. (1994)
N V	Liang & Badnell 2011)
O I	Bell et al. (1998)
O I	Zatsarinny & Tayal (2003)
O II	Tayal (2007)
O III	Palay et al. (2012)
O IV	Blum & Pradhan (1992)
O V	K. A. Berrington (2003, private communication)
O V	Bhatia & Landi (2012)
O VI	Liang & Badnell (2011)
Ne III	Landi & Bhatia (2005)
Ne IV	Ramsbottom et al. (1998)
Ne V	Badnell & Griffin (2000)
Si III	Galavís et al. (1995)
Si III	Galavís et al. (1998)
Si III	Mendoza & Zeippen (1982)
S II	Tayal & Zatsarinny (2010)
S III	Hudson et al. (2012)
Ca V	Galavís et al. (1995)
Fe II	Nussbaumer & Storey (1980)
Fe II	Nussbaumer & Storey (1988)

For a κ-distribution, the corresponding rate is

$$R_{12}(\kappa) = n_e N_1 \frac{h^2}{4\pi^{3/2} m_e g_1} \frac{\Gamma(\kappa+1)}{\left(\kappa-\frac{3}{2}\right)^{3/2}\Gamma\left(\kappa-\frac{1}{2}\right)} (k_B T_U)^{-3/2} \times \int_{E_{12}}^{\infty} \frac{\Omega_{12}(E)}{\left(1+E\Big/\left[\left(\kappa-\frac{3}{2}\right)k_B T_U\right]\right)^{\kappa+1}} dE, \qquad (3)$$

where E_{12} is the energy gap between levels 1 and 2, g_1 is the statistical weight of the lower state, and Γ is the gamma function.

If the detailed collision strengths, $\Omega(E)$, are known, Equations (2) and (3) can be integrated numerically and the κ collisional excitation rate can be expressed in terms of the M–B collisional excitation rate.

As a first order approximation, we can assume that the collision strength for excitations from level 1 to 2, Ω_{12}, is independent of energy. For this case, the ratio of the rates of collisional excitation from level 1 to level 2 for a κ-distribution can be expressed analytically (Nicholls et al. 2012) as:

$$\frac{R_{12}(\kappa)}{R_{12}(\mathrm{M-B})} = \frac{\Gamma(\kappa+1)}{\left(\kappa-\frac{3}{2}\right)^{3/2}\Gamma\left(\kappa-\frac{1}{2}\right)} \left(1-\frac{3}{2\kappa}\right) \times \exp\left[\frac{E_{12}}{k_B T_U}\right] \left(1+\frac{E_{12}}{\left(\kappa-\frac{3}{2}\right)k_B T_U}\right)^{-\kappa}. \qquad (4)$$

This equation can be evaluated analytically as a series of concave "banana curves" (see Nicholls et al. 2012, Figure 5).

When collision strengths are computed, in some cases *only* the "effective collision strengths," $\Upsilon_{\mathrm{M-B}}(T)$, computed assuming

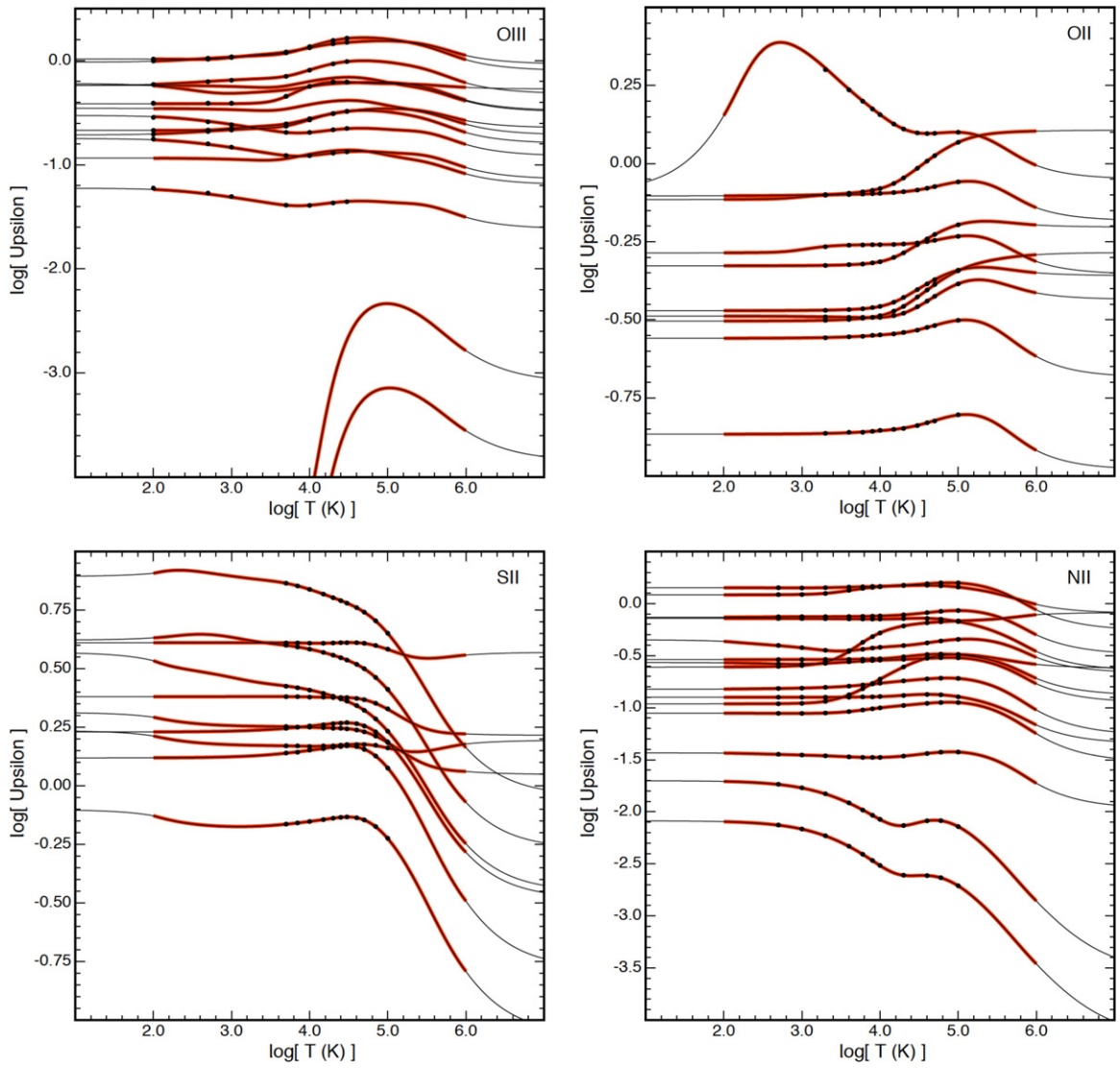

Figure 1. Effective energy-averaged collision strengths, Υ, for an M–B electron energy distribution computed for the lowest transitions for O III, O II, S II, and N II. The dots are the values published in the literature, the thick red lines are our computations made at high energy resolution using Equation (6), and the thin black lines are our spline fits to these high resolution data. Note that our interpolation scheme produces well-behaved asymptotes in both the high- and low-temperature limits.
(A color version of this figure is available in the online journal.)

M–B equilibrium electron energies, are published:

$$\Upsilon_{\text{M-B}}(T) = \frac{\int_{E=E_{12}}^{\infty} \Omega_{12}(E) \exp\left(\frac{-E}{kT}\right) d\left(\frac{E}{kT}\right)}{\int_{E=E_{12}}^{\infty} \exp\left(\frac{-E}{kT}\right) d\left(\frac{E}{kT}\right)}. \quad (5)$$

Where data on the detailed energy dependence of Ω are not available, a reasonable approximation for the effective collision strengths Υ_κ for a κ-distribution can be calculated in terms of the equilibrium effective collision strengths $\Upsilon_{\text{M-B}}$ using Equation (4):

$$\Upsilon_\kappa = \frac{R_{12}(\kappa)}{R_{12}(\text{M}-\text{B})} \Upsilon_{\text{M-B}}. \quad (6)$$

Equation (6) allows us to compute the κ dependence of the collisional excitation in terms of that for an equilibrium energy distribution, even where complete data on Ω are not available.

In the revised MAPPINGS code, as described above, where detailed data for Ω are available (see Nicholls et al. 2013), we compute the effective collision strengths Υ for temperatures between 10^3 and 10^7 K and express the effective κ collision strengths Υ_κ in terms of the equilibrium $\Upsilon_{\text{M-B}}$ s. Where only M–B-averaged effective collision strengths are available, we compute κ values using Equation (6).

To demonstrate the accuracy of the procedures used, we show in Figure 1 the equilibrium effective collision strengths for the lowest 10 or 15 transitions for the ions O III, O II, S II, and N II. The dots are the values as published in the literature (see Table 1), the thick red lines represent the high temperature resolution computations using Equation (6), and the thin black lines are the spline fits to the high resolution data, calculated as described earlier.

In Figure 2, we show the effective collision strengths for the $^3P_2$–$^1D_2$ and $^3P_2$–$^1S_0$ transitions in [O III]. M3 indicates the collision strengths used in the previous version of MAPPINGS and M4 indicates the latest versions. κ10 shows the effective collision strengths for a non-equilibrium electron energy distribution with $\kappa = 10$. While the $^3P_2$–$^1D_2$ values are reasonably similar between $10^{3.5}$ and 10^4 K, at lower temperatures the divergence is considerable between the older version and the new MAPPINGS data. Extrapolating the older MAPPINGS data

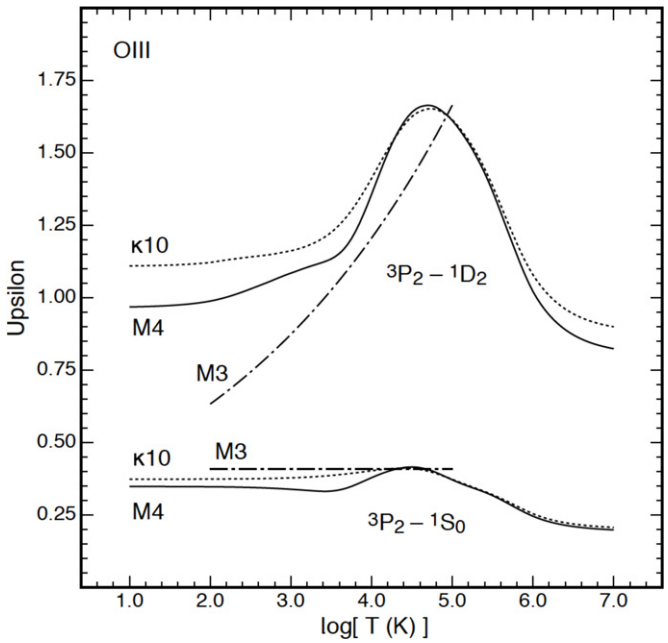

Figure 2. Effective collision strengths for equilibrium (M3 and M4) and $\kappa = 10$ electron energy distributions (κ10), for the $^3P_2$–$^1D_2$ and $^3P_2$–$^1S_0$ transitions in [O III]. M3 indicates the effective collision strengths used in the previous version of MAPPINGS, and M4 indicates the new values. The differences are greatest at low temperature in the $^3P_2$–$^1D_2$ transition, producing the greatest effect in high-abundance H II regions.

above 10^5 K is likely to give severe errors. These differences are likely to produce significant effects in models of X-ray ionized nebulae or models of the emission spectrum of material entering shock fronts.

3. THE MODEL GRID

3.1. Abundance Set and Dust Physics

The solar abundance set is taken from Grevesse et al. (2010) and the depletion factors for each element are updated from Dopita et al. (2005) using the data from Kimura et al. (2003). These values are listed in Table 2. The elemental depletion results from condensation of the heavy elements onto dust grains. The treatment of dust grain composition, size distribution and absorption properties adopted here is essentially identical to that used in MAPPINGS 3 and is described in detail in Dopita et al. (2005). Suffice it to say here that within the ionized region, our dust model has silicate grains following a Mathis et al. (1977) size distribution and a population of small carbonaceous grains. The polycyclic aromatic hydrocarbon molecules are assumed to be destroyed within the ionized H II region (although they are present in the photodissociation regions around the periphery of the H II region). The effects of radiation pressure acting on dust (Dopita et al. 2002) and photoelectric heating due to grain photoionization (Dopita & Sutherland 2000) are fully taken into account in the models.

A perennial problem with fitting the spectrum of H II regions over a wide range of abundances is the question of how to deal with the N and C abundances. Both of these elements contain a primary nucleosynthetic contribution as well as a secondary nucleosynthetic source that becomes important at higher abundances. In Dopita et al. (2000), the transition from primary to secondary element was treated as more or less abrupt, but this method does not conform to the extensive

Table 2
Solar Abundance Set ($Z_\odot$) and the Logarithmic Depletion Factors (D) Adopted for Each Element

Element	$\log(Z_\odot)$	$\log(D)$
H	0.00	0.00
He	−1.01	0.00
C	−3.57	−0.30
N	−4.60	−0.05
O	−3.31	−0.07
Ne	−4.07	0.00
Na	−5.75	−1.00
Mg	−4.40	−1.08
Al	−5.55	−1.39
Si	−4.49	−0.81
S	−4.86	0.00
Cl	−6.63	−1.00
Ar	−5.60	0.00
Ca	−5.66	−2.52
Fe	−4.50	−1.31
Ni	−5.78	−2.00

Table 3
The C and N Abundances as a Function of O/H

12 + log (O/H)	log (N/H)	log (C/H)
7.39	−6.61	−5.58
7.50	−6.47	−5.44
7.69	−6.23	−5.20
7.99	−5.79	−4.76
8.17	−5.51	−4.48
8.39	−5.14	−4.11
8.69	−4.60	−3.57
8.80	−4.40	−3.37
8.99	−4.04	−3.01
9.17	−3.67	−2.64
9.39	−3.17	−2.14

Note. Solar: 12 + log(O/H) = 8.69.

observationally derived data of van Zee et al. (1998) (for the N/O ratio) or the data of Garnett et al. (2004), and references therein, for both N/O and C/O. In this work, we have adopted an empirical smooth function variation in both N/H and C/H as a function of O/H. These abundances are listed in Table 3 and the fit for the adopted N/O ratio as a function of O/H is shown in Figure 3, for comparison with the van Zee et al. (1998) data set. Note the increased scatter at the low abundance end, which may be of some importance to the accuracy of the strong-line abundance diagnostics developed in this paper for $12 + \log(\mathrm{O/H}) < 8.4$.

For helium, we adopt a similar prescription as used by Dopita et al. (2002), which provides a good fit to the He abundances observed in H II regions. This prescription adds the primary production of He to the primordial He abundance. By number of atoms:

$$\frac{\mathrm{He}}{\mathrm{H}} = 0.0737 + 0.024\frac{Z}{Z_\odot}.$$

3.2. Stellar Model Atmospheres

The stellar model atmospheres are based upon the STARBURST99 code of Leitherer et al. (1999). Here, we have assumed a Salpeter initial mass function (IMF), $dN/dm \propto m^{-2.35}$, with a lower mass cutoff of 0.1 $M_\odot$ and an upper mass cutoff of 120 $M_\odot$, as described in Dopita et al. (2000). We have

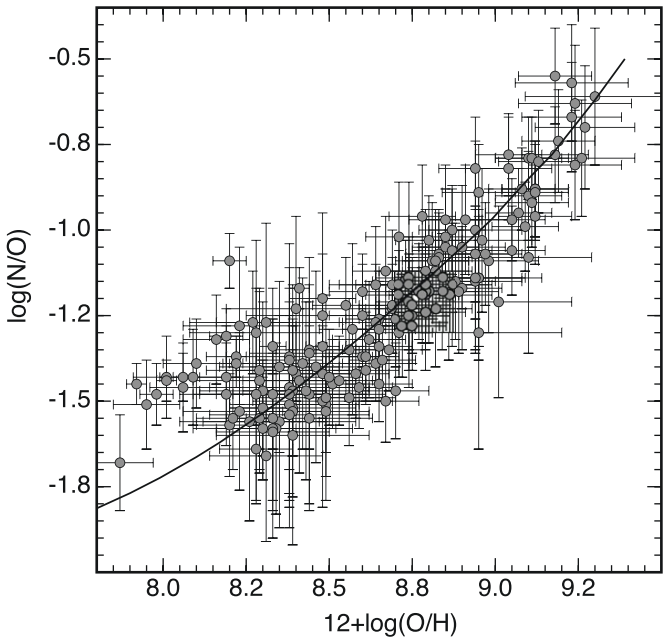

Figure 3. Relationship between the oxygen abundance, 12 + log(O/H), and the N/O ratio for the H II regions observed by van Zee et al. (1998). The functional relationship adopted in the models is indicated as a solid line and is tabulated in Table 3. The accuracy of this calibration is central to the accuracy of the new strong-line diagnostics developed in this paper. Note that the increased scatter at the low abundance end may pose an issue in the determination of the chemical abundances of low-abundance H II regions.

used the Lejeune et al. (1997) model atmospheres. For stars with strong winds, we switch to the Schmutz et al. (1992) extended model atmospheres using the prescription of Leitherer & Heckman (1995). We assume that typical H II regions are excited by a cluster with continuous star formation extending over 4 Myr. This approximation agrees with observed H II regions since there is a strong bias toward observing the younger H II regions, which have in general higher densities, much higher emissivities, and larger absolute Hα fluxes (Dopita et al. 2006a). The models also provide a good approximation to the typical age spread of the stars observed in luminous clusters exciting bright H II regions (Beccari et al. 2000; De Marchi et al. 2011).

We have elected to use the earlier STARBURST99 models used by Dopita et al. (2000), as they provide a harder radiation field than the models generated by more recent versions of the code. These newer models incorporate fully self-consistent radiatively driven atmospheres, but they generate an EUV radiation field that is rather too soft to reproduce the H II region sequence (Dopita et al. 2006b). The most likely reason for this fact is that the stellar winds of OB stars are clumpy rather than smooth, which assists the escape of EUV photons.

A small difficulty with the STARBURST99 models is that the "solar" metallicity models do not correspond to the Grevesse et al. (2010) abundance set. For oxygen in particular, the 12 + log(O/H) default solar abundance has changed from 8.86 to 8.69—nearly a factor of two lower. Thus, for most of the abundance sets that we would like to compute, the corresponding STARBURST99 models are missing. To account for this fact, we generated stellar model atmospheres by linear interpolation of the logarithmic fluxes at any given frequency between the nearest adjacent STARBURST99 models in metallicity, by assuming that the logarithm of the flux varies in proportion to 12 + log(O/H). This technique allows us to construct a more finely sampled grid of models in which the stellar and the nebular chemical abundances are effectively identical, with the exception of the case 0.05 $Z_\odot$, where the atmosphere used is simply the lowest that can be obtained from the STARBURST99 code; this case corresponds to 12 + log(O/H) $\sim$ 7.56 rather than 7.39.

4. A REFERENCE CATALOG OF H II REGION MODELS

We have run a grid of spherical, isobaric H II region models at 5.0, 3.0, 2.0, 1.0, 0.5, 0.3, 0.2, 0.1, and 0.05 $Z_\odot$, where the solar abundance corresponds to 12 + log(O/H) = 8.69. The full set of elemental abundances for solar abundance are listed in Table 2. The models were terminated when more than 95% of the hydrogen has recombined, and the temperature has fallen to less than 2000 K. The pressure in the models was set at $P/k = 10^5$, typical of bright H II regions in external galaxies. The density of these models, $n \sim 10$ cm^{-3}, is fixed by the pressure, and is typical of giant extragalactic H II regions. We do not need to consider models of different densities since, at the densities typically encountered in these H II regions, collisional de-excitation is unimportant.

The ionization parameter, log(q)[4], was fixed by its value at the inner boundary of the H II region. For each set of abundances, log(q) ran from 8.5 down to 6.5 in steps of 0.25. Because these are spherical models, the radial divergence of the radiation field and attenuation of the radiation field by absorption in the ionized plasma within the models is important, especially at high ionization parameter. By contrast, the low log(q) models approximate a thin shell of ionized gas. As an example, for the log(q) = 8.5 model at solar abundance, the mean ionization parameter in the ionized hydrogen is only log$\langle q\rangle$ = 7.95, while for the log(q) = 6.5 model at solar abundance, the mean ionization parameter in the ionized hydrogen is log$\langle q\rangle$ = 6.42.

The full log(q) : Z grid was run for several different values of κ = 10, 20, 50, and ∞ (which corresponds to the standard M–B case), giving a complete family of 324 models covering the three independent variables that control the strong-line emission spectrum. The lines relevant to the abundance diagnostics, as well as those relevant for measuring electron temperatures in the nebulae, are tabulated in Tables 4 (the "blue" lines) and 5, which lists the lines in the red and near-IR portions of the spectrum. In these tables, all line intensities are expressed as a fraction of the Hβ intensity, to four significant figures. In the original models, the line fluxes are computed down to any intensity, but the spectral line list for each model gives lines with $F > 10^{-6}$ that of Hβ. This procedure allows an accurate computation of the effective forbidden line temperatures down to $T_e \sim 3000$ K.

In order to compute the effective forbidden emission line temperatures, $T_{\rm FL}$, for the ions O III, Ar III, S III, O II, N II, and S II we have used the integrated line fluxes given by the models along with the fitting formulae given by Nicholls et al. (2013), which were obtained using the same atomic data. The temperature sensitive ratios used are as follows: [O III] λ4363/λ5007, [Ar III] λ5192/λ7751, [S III] λ6312/λ9069, [O II] λ7318, 30/λ3727, 9, [N II] λ5755/λ6584, and [S II] λ4068, 76/λ6731.

In addition to the forbidden line temperatures, we have computed the effective recombination temperatures from the average ionic kinetic (or internal energy) temperatures, $T_{\rm U}$, in

[4] The dimensionless ionization parameter $\mathcal{U}$ measures the ratio of the density per unit volume of ionizing photons to the particle (atom plus ion) number density. In this paper, we use the alternative definition, q, which is defined as the ratio of the number of ionizing photons impinging per unit area per second divided by the gas particle number density. The transformation between the two definitions is simply $\mathcal{U} = q/c$, c being the speed of light.

Table 4
The "Blue" Line Fluxes Given by the MAPPINGS 4 Models Relative to $F_{H\beta} = 1.0$

log(q)	[O II] 3727	[O II] 3729	[Ne III] 3869	[S II] 4068, 78	Hγ 4340	[O III] 4363	He I 4471	Hβ 4861	[O III] 4959	[O III] 5007	He I 5016	[Ar III] 5192	[N I] 5198, 00	[N II] 5755
						$5.0\,Z_\odot; \kappa = \infty$								
8.50	0.0105	0.0148	0.0002	0.0003	0.4447	0.0000	0.0941	1.0000	0.0021	0.0061	0.0529	0.0000	0.0000	0.0001
8.25	0.0067	0.0095	0.0001	0.0002	0.4458	0.0000	0.0923	1.0000	0.0014	0.0039	0.0498	0.0000	0.0000	0.0000
8.00	0.0048	0.0068	0.0001	0.0002	0.4470	0.0000	0.0907	1.0000	0.0010	0.0029	0.0472	0.0000	0.0000	0.0000
7.75	0.0039	0.0055	0.0001	0.0002	0.4481	0.0000	0.0889	1.0000	0.0008	0.0023	0.0452	0.0000	0.0000	0.0000
7.50	0.0030	0.0043	0.0001	0.0002	0.4488	0.0000	0.0873	1.0000	0.0006	0.0017	0.0438	0.0000	0.0000	0.0000
7.25	0.0019	0.0027	0.0000	0.0001	0.4486	0.0000	0.0841	1.0000	0.0003	0.0010	0.0423	0.0000	0.0000	0.0000
7.00	0.0008	0.0012	0.0000	0.0001	0.4472	0.0000	0.0793	1.0000	0.0001	0.0004	0.0407	0.0000	0.0000	0.0000
6.75	0.0003	0.0004	0.0000	0.0000	0.4442	0.0000	0.0728	1.0000	0.0000	0.0001	0.0396	0.0000	0.0000	0.0000
6.50	0.0000	0.0001	0.0000	0.0000	0.4394	0.0000	0.0635	1.0000	0.0000	0.0000	0.0392	0.0000	0.0000	0.0000

(This table is available in its entirety in a machine-readable form in the online journal. A portion is shown here for guidance regarding its form and content.)

Table 5
The "Red" Line Fluxes Given by the MAPPINGS 4 Models Relative to $F_{H\beta} = 1.0$

log(q)	He I 5875	[O I] 6300	[S III] 6312	[N II] 6548	Hα 6563	[N II] 6584	He I 6678	[S II] 6717	[S II] 6731	[Ar III] 7136	[O II] 7318, 30	[Ar III] 7751	[S III] 9068	[S III] 9532
						$5.0\,Z_\odot; \kappa = \infty$								
8.50	0.3218	0.0012	0.0001	0.0565	3.3420	0.1661	0.0880	0.0267	0.0188	0.0052	0.0000	0.0013	0.0559	0.1403
8.25	0.3130	0.0010	0.0001	0.0472	3.3210	0.1387	0.0863	0.0259	0.0182	0.0044	0.0000	0.0011	0.0488	0.1227
8.00	0.3037	0.0010	0.0000	0.0429	3.2950	0.1263	0.0844	0.0277	0.0194	0.0042	0.0000	0.0010	0.0457	0.1147
7.75	0.2942	0.0011	0.0000	0.0422	3.2730	0.1243	0.0823	0.0322	0.0226	0.0045	0.0000	0.0011	0.0447	0.1122
7.50	0.2865	0.0012	0.0000	0.0416	3.2580	0.1223	0.0804	0.0375	0.0263	0.0047	0.0000	0.0011	0.0422	0.1059
7.25	0.2758	0.0011	0.0000	0.0355	3.2660	0.1044	0.0775	0.0378	0.0266	0.0040	0.0000	0.0010	0.0339	0.0851
7.00	0.2620	0.0008	0.0000	0.0235	3.3000	0.0692	0.0733	0.0298	0.0210	0.0026	0.0000	0.0006	0.0209	0.0525
6.75	0.2449	0.0005	0.0000	0.0124	3.3670	0.0365	0.0678	0.0187	0.0132	0.0012	0.0000	0.0003	0.0099	0.0248
6.50	0.2206	0.0002	0.0000	0.0035	3.4790	0.0103	0.0597	0.0065	0.0046	0.0002	0.0000	0.0001	0.0025	0.0063

(This table is available in its entirety in a machine-readable form in the online journal. A portion is shown here for guidance regarding its form and content.)

Table 6
The Recombination and Forbidden Line Temperatures of the MAPPINGS 4 Models

log(q)	T_H	T_{He}	$T_{[O III]}$	$T_{[Ar III]}$	$T_{[S III]}$	$T_{[O II]}$	$T_{[N II]}$	$T_{[S II]}$
				$5.0\,Z_\odot; \kappa = \infty$				
8.50	2706	2506	···	···	3814	3721	3953	3599
8.25	2729	2562	···	···	3586	3508	3720	3423
8.00	2799	2682	···	···	3407	3359	3538	3279
7.75	2889	2824	···	···	3266	3007	3397	3168
7.50	2950	2928	···	···	3133	2987	3248	3052
7.25	2918	2932	···	···	2977	···	3051	2898
7.00	2756	2807	···	···	2804	···	2833	2717
6.75	2481	2561	···	···	···	···	···	2574
6.50	2026	2117	···	···	···	···	···	2373

(This table is available in its entirety in a machine-readable form in the online journal. A portion is shown here for guidance regarding its form and content.)

the H^+ and He^+ zones. In a κ-distribution, the M–B "core," which determines the energy distribution of the recombining electrons, and hence the recombinations, occurs at a lower effective temperature, T_{rec}, than the internal energy temperature, $T_{rec} = T_U(1 - 3/2\kappa)$ (Nicholls et al. 2012, 2013). We must therefore correct the average ionic kinetic temperatures given by the code by this factor.

The complete list of nebular temperature estimates is given in Table 6. Figure 4 shows the way in which metallicity, ionization parameter, and κ all affect the measured line temperatures ($T_{[O III]}$ and $T_{[O II]}$), as well as the hydrogen recombination temperature (T_{rec}). Some general observations can be made about this fact. First, as is well known, low-abundance H II regions have higher temperatures than high-abundance H II regions. Second, the electron temperature is usually positively correlated with $\log q$. Third, $T_{[O III]}$ is generally higher than $T_{[O II]}$.

Figure 4 also shows the way in which κ influences the effective (as measured) forbidden emission line temperatures, T_{FL}, and the hydrogen recombination temperature T_{rec}. In the presence of a κ-distribution, T_{rec} is always lowered, while T_{FL} is usually (but not always) raised. The lower T_{rec} will result in generally stronger recombination lines. This result may in turn lead to an overestimate of the chemical abundances derived from recombination lines when temperatures derived from the forbidden lines are used to interpret the recombination line intensities.

5. WHAT IS THE LIKELY VALUE OF κ?

As Figure 4 shows, the most sensitive dependence with κ is found in the difference between the forbidden line temperatures, T_{FL}, and the hydrogen recombination temperature T_{rec}. The helium recombination temperature could equally well be used in the place of the hydrogen recombination temperature, since the difference between the two is small for all models (see Table 6).

The high quality échelle spectroscopy of Galactic and extragalactic H II regions shows that there is indeed a systematic a difference between T_{FL} and T_{rec}. Here, we have collected data on

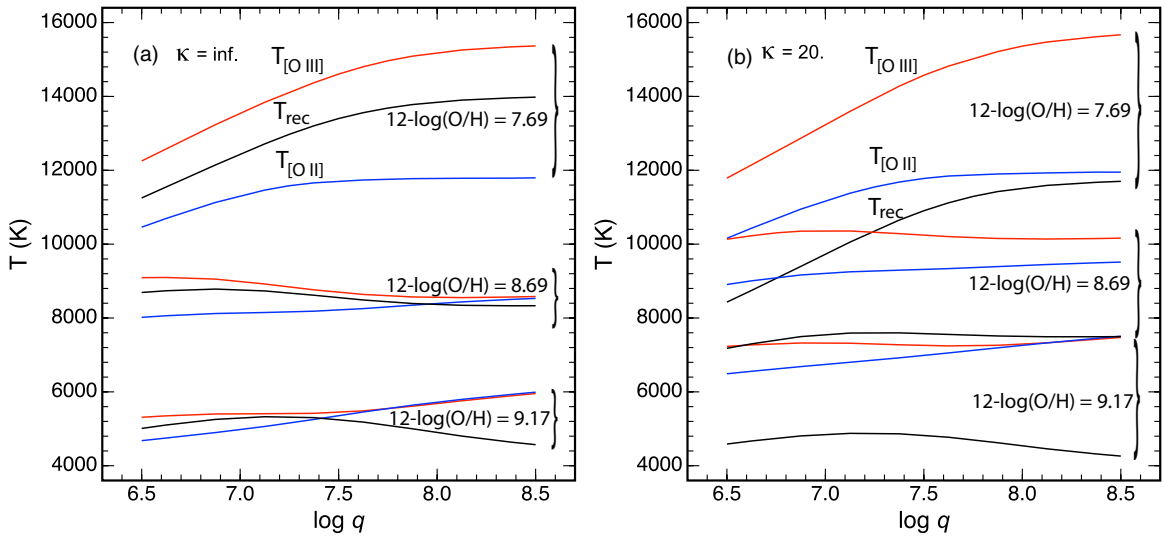

Figure 4. Relationship between the forbidden line and recombination line temperatures as a function of $\log q$ and chemical abundance. The left-hand panel shows models with a Maxwell–Boltzmann electron distribution, while the right-hand panel shows the case $\kappa = 20$. The red lines indicate the temperature in the high-ionization zone of the H II region, $T_{[\mathrm{O\,III}]}$, the blue lines indicate the temperature in the low-ionization zone of the H II region, $T_{[\mathrm{O\,II}]}$, and the black lines indicate the hydrogen recombination temperature T_{rec}. For all models, the effect of κ is to raise $T_{[\mathrm{O\,III}]}$ and lower T_{rec}. However, $T_{[\mathrm{O\,II}]}$ may either be higher (at high Z) or slightly lowered (at low Z).

(A color version of this figure is available in the online journal.)

Galactic H II regions from M42 (Esteban et al. 2004), NGC 3576 (García-Rojas et al. 2005a), S311 (García-Rojas et al. 2005b), M20 & NGC 3602 (García-Rojas & Esteban 2006), and M8 & M17 (García-Rojas & Esteban 2007). For the extragalactic H II regions, we have data for 30 Dor (Peimbert 2003), NGC 595 (López-Sánchez et al. 2007), NGC 595, NGC 604, VS 24, VS 44, NGC 2365, and K 932 (Esteban et al. 2009). However, instead of using the forbidden line temperatures given by these authors, we have used the measured fluxes and made an independent estimate of the temperatures implied by these fluxes using the Nicholls et al. (2013) analytic equations. This method ensures that the derived temperatures are consistent with the new atomic data used here. Noting that the helium recombination temperatures and the hydrogen recombination line temperatures are very similar, we have used the average of these (when available) to estimate T_{rec}. In the absence of either, we have used the other to give our estimate of T_{rec}. The error bars on the temperatures are assumed to be the same as those given by the authors cited above.

It should be noted that, in all cases, the temperatures are derived for only a small patch of the total H II region. These "pencil-beam" observations therefore do not provide a temperature that is representative of the nebula as a whole. This issue may be a problem when comparing the data with the models.

With these data, we have constructed Figure 5, which shows forbidden line temperatures plotted for two ions arising in the high-ionization zones of H II regions, O III and Ar III, and two ions arising in the low-ionization zones, O II and N II, compared with the recombination temperatures as derived above. In general, the κ-distribution models provide a better fit than the M–B case. There may well be an intrinsic scatter in κ appropriate to individual H II regions. However, the data are mostly consistent with a fairly moderate $\kappa \sim 20$, or somewhat higher. This result represents only a very mild deviation from the M–B case, but it is sufficient to significantly affect our estimates of forbidden line and recombination temperatures. In the analysis that follows, we will adopt $\kappa \sim 20$.

6. EFFECT OF κ ON UV AND IR LINES

6.1. The UV Lines of Carbon

The UV spectrum of H II regions is rather sparse (Garnett et al. 1995b) and, as a consequence, only a few observations have been obtained in this wavelength region, mostly by Garnett and his collaborators (Garnett et al. 1995a, 1999). The strongest lines are generally the C III] λλ1906, 9 doublet and the C II] λ2326 multiplet. The Si III] λλ1883, 92 lines are sometimes seen, as well as the [O II] λλ2470 line.

Here, we will consider only the effect of the κ-distribution on the important carbon lines. The effect on the Si III] λλ1883, 92 lines is essentially the same as on the C III] λλ1906, 9 doublet, and the effect on the [O II] λλ2470 line is similar to that on the C II] λ2326 multiplet. In Figure 6, we plot the enhancement in the line intensity for $\kappa = 20$ compared with $\kappa = \infty$, against the predicted line flux relative to Hβ computed for models with $\kappa = \infty$. The enhancement in the line intensity is very significant for metallicities greater than two times solar. The reason for these large correction factors is that the temperature of the H II region is low and the hot tail in the κ electron energy distribution becomes very important. However, there are no UV measurements for H II regions in this metallicity range, so the computations cannot be checked. For lower metallicities, the corrections are much smaller, and the carbon lines are generally affected by less than a factor of two. Nonetheless, these corrections may well be important where UV lines are being used to estimate the C/O ratio.

6.2. The IR Lines

In contrast with the UV, the effect of κ on the IR lines is very weak indeed. At the high abundance end, the intensities of the strong lines are weakened by only 2%–4%, even at $\kappa = 10$. The effect becomes more noticeable for low abundance H II regions, with line intensities being weakened by as much as 25%. This result is easily understood by referencing to the "banana curves"

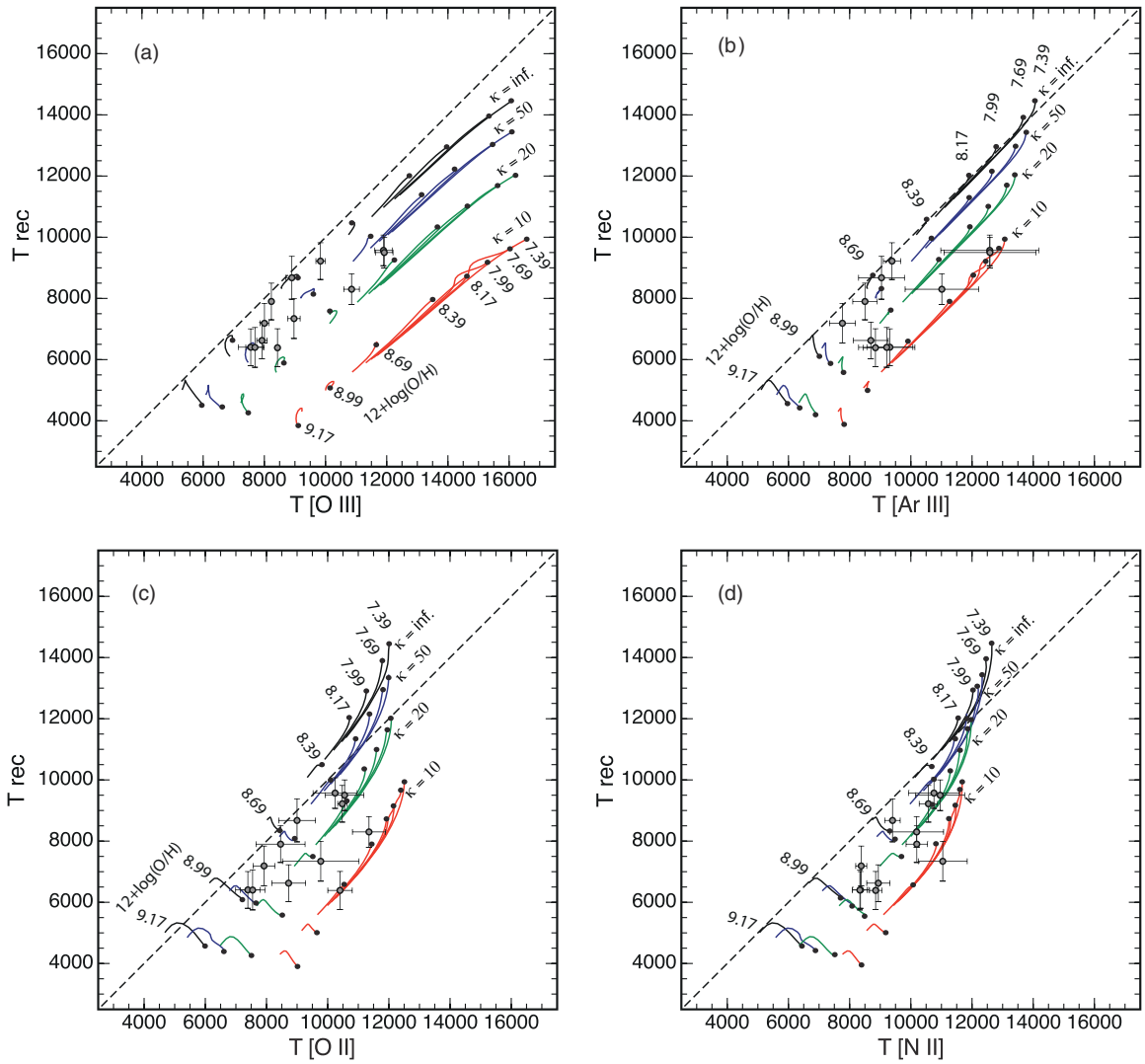

Figure 5. Relationship between the forbidden line and recombination line temperatures. The observations for the Galactic and extragalactic H II regions derived from the high-quality échelle data cited in the text are shown with error bars. The models at each abundance, and for each set of $\log q$, are shown as "worms" in which the head represents $\log q = 8.5$ and the tail represents $\log q = 6.5$. Each value of κ is coded by color, as indicated. Note the difference in behavior between the ions arising in the high-ionization zones of the H II region: O III and Ar III (panels (a) and (b)), and those arising from the low-ionization regions, O II and N II (panels (c) and (d)). From this figure, we conclude that the best-fit value of κ is ~20, or possibly somewhat higher.

(A color version of this figure is available in the online journal.)

of Nicholls et al. (2012, 2013), which show that only weak κ-related changes are expected in the excitation rates of the IR lines for typical nebular temperatures.

More problematic is the fact that the models do not give a very good description of the observed spectrum of H II regions. Snijders et al. (2007) compared the MAPPINGS models with the observations of Giveon et al. (2002) and devised two new mid-IR diagnostics based on the excitation-dependent ratios [Ne III] 15.56 μm/[Ne II] 12.81 μm, [S IV] 10.51 μm/[S III] 18.71 μm, [S III] 18.71 μm/[Ne II] 12.81 μm, and [S IV] 10.51 μm/[Ar III] 8.99 μm. In Figure 7, we plot one of these diagnostics: the [Ne III] 15.56 μm/[Ne II] 12.81 μm versus [S IV] 10.51 μm/[S III] 18.71 μm and a new one, [Ne III] 15.56 μm/[Ne II] 12.81 μm versus /[Ar III] 8.99 μm/[Ne II] 12.81 μm, along with the Giveon et al. (2002) data. Here, the grids are shown only for $\kappa = \infty$—the grids for $\kappa = 20$ fully overlap these grids.

The offsets between the theory and the observations require explanation. First, let us consider the possibility that the intensity of the [Ne II] 12.81 μm line is in error. If this fact were the case, the grid on the left-hand side of Figure 7 would move closer to the observations. However, the effect on the right-hand side of the diagram would simply be to translate the curve along the 45 deg line, leading to no improvement here. Likewise, the [Ne III] 15.56 μm line intensity cannot be the source of the problems, since changing this lines translates both grids sideways in the same direction, so the fit of one is improved only at the expense of the other.

A more likely explanation is that the [S IV] 10.51 μm/[S III] 18.71 μm ratio is in error, particularly at the high abundance end. Snijders et al. (2007) showed that a much better fit between observations and theory can be obtained if the mean effective age of the exciting clusters is somewhat older than we have used here. This older age allows an appreciable population of Wolf–Rayet stars to develop. These stars have higher effective temperatures, can excite species with higher ionization potentials, and so produce more S IV ions in the nebula, resulting in a stronger [S IV] 10.51 μm line. To explain the offset in the [Ar III] 8.99 μm/[Ne II] 12.81 μm ratio, we would have to appeal to errors in either the atomic data for the [Ar III] line or else errors in the charge-exchange rates that

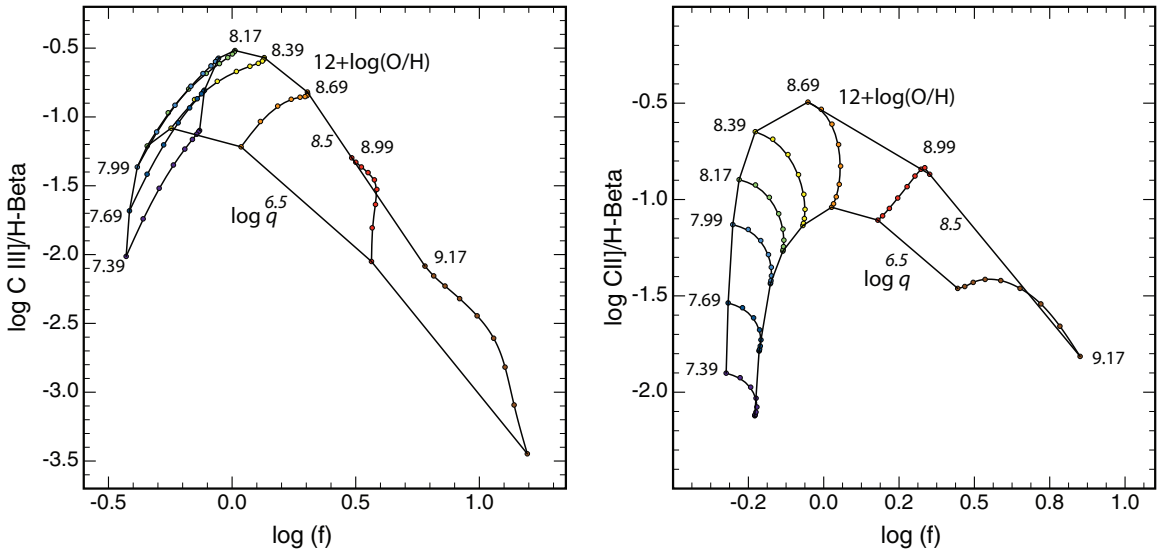

Figure 6. Effect of $\kappa = 20$ on the C III] $\lambda\lambda$1906, 9 doublet (left), and the C II] λ2326 multiplet (right). The vertical axis is the predicted line flux relative to Hβ for $\kappa = \infty$ and the horizontal axis is the factor, f, by which the line intensity has to be multiplied to give the predicted intensity for $\kappa = 20$. The effect of κ is most evident at high abundance, where line intensities may be enhanced by as much as a factor of 10.

(A color version of this figure is available in the online journal.)

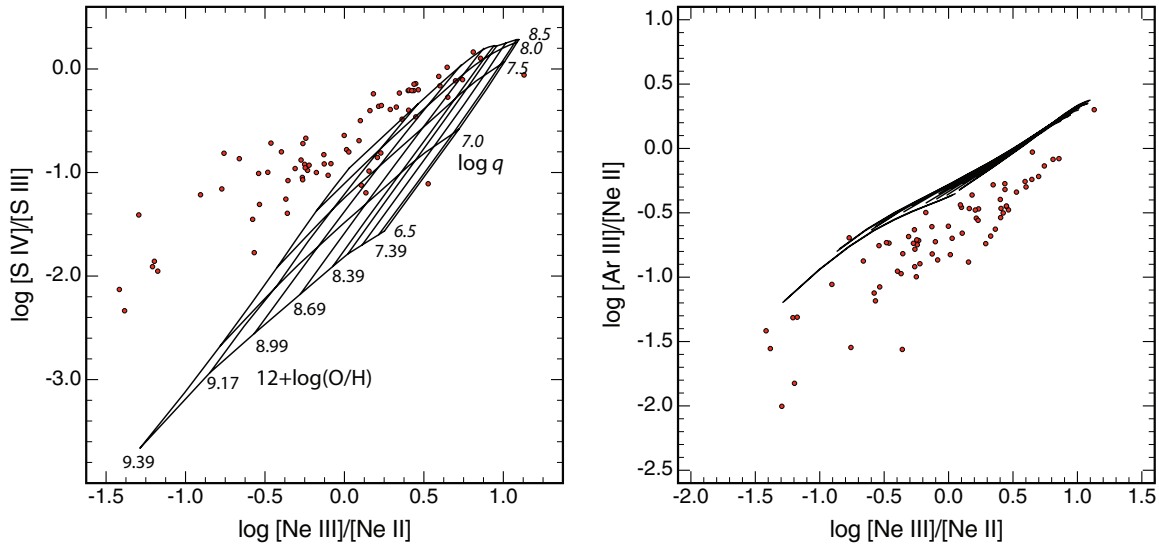

Figure 7. Mid-IR diagnostics, [S IV] 10.51 μm/[S III] 18.71 μm (left) vs. [Ne III] 15.56 μm/[Ne II] 12.81 μm, and [Ar III] 8.99 μm/[Ne II] 12.81 μm (right) vs. [Ne III] 15.56 μm/[Ne II] 12.81 μm plotted for $\kappa = \infty$. The points represent the Giveon et al. (2002) data for Galactic and Magellanic Cloud H II regions. The probable cause of the offset between theory and observations is discussed in the text.

(A color version of this figure is available in the online journal.)

strongly affect the ionization balance of Ar. All of these issues point to the need for more work in refining the predictions of models in the IR.

In the far-IR, we have identified a very promising abundance—ionization parameter diagnostic. This diagnostic is shown in Figure 8 where we plot [N III] 57.34 μm/[O III] 51.81 μm versus [O IV] 25.89 μm/[O III] 51.81 μm, as delivered by the models. This grid is little affected by κ and provides a very clean separation between the abundance and the ionization parameter.

7. STRONG LINE RATIO DIAGNOSTICS

7.1. Veilleux and Osterbrock Diagnostics

Following the pioneering work of Baldwin et al. (1981), Veilleux & Osterbrock (1987, VO87) exploited the utility of diagnostics based on the ratio of the strong red lines [N II]/Hα, [S II]/Hα, and [O I]/Hα plotted against the ratio [O III] λ5007/Hβ. These ratios have the great advantage of using lines close together in wavelength, so that the reddening correction for dust is negligible. VO87 noted that the H II regions are confined to a rather narrow strip on these diagrams, while Seyferts and low-ionization nuclear emission-line regions (LINERs) lay systematically above and to the right, respectively, of the H II region sequence. These diagrams are therefore of great utility in determining the mode of excitation for photoionized objects. The permitted H II region and starburst region was established by Kauffmann et al. (2003) and the formal division between the starburst, Seyfert, and LINER zones on these diagrams was established empirically by Kewley et al. (2006) using very extensive Sloan Digital Sky Survey (SDSS) spectrophotometry.

A number of theoretical attempts have been made to reproduce the narrow H II region and starburst sequence. Dopita et al. (2000) demonstrated that the narrowness of the sequence

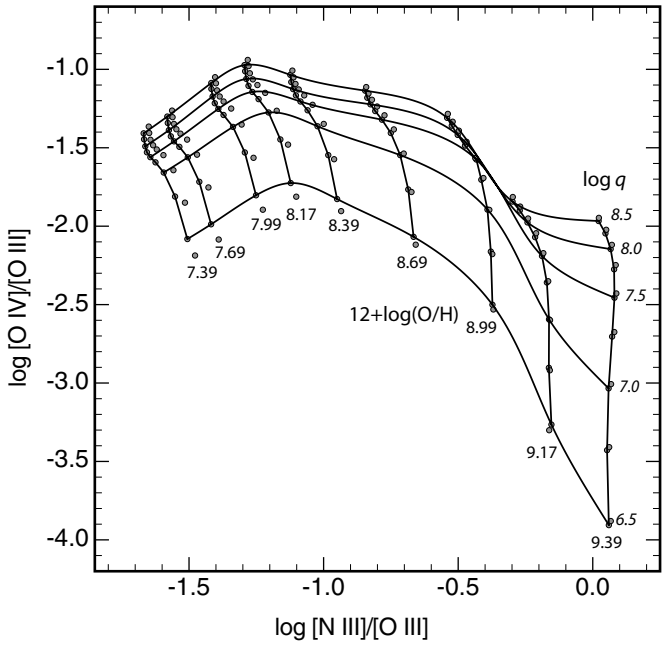

Figure 8. Far-IR diagnostic for abundance and ionization parameter, [O IV] 25.89 μm/[O III] 51.81 μm vs. [N III] 57.34 μm/[O III] 51.81 μm. The grid is shown for $\kappa = \infty$ and the gray circles represent the $\kappa = 20$ case. The effect of κ on this diagnostic is very small.

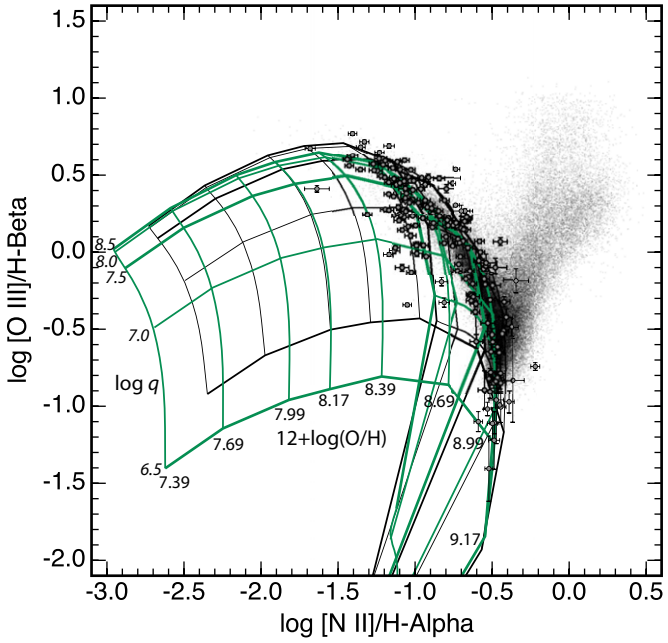

Figure 9. VO87 plot of [O III] λ5007/Hβ vs. [N II] λ6584/Hα. The grey dots represent the SDSS data set as used by Kewley et al. (2006), while the points with error bars are from the van Zee et al. (1998) data set. The delineation of the two AGN sequences in the upper right-hand side of the diagram, the Seyferts (upper) and LINERS (lower), is very clear on this plot. The models grids on this and all subsequent diagnostic diagrams are shown for two values of κ: $\kappa = \infty$ (black lines) and $\kappa = 20$ (green lines). Note that the effect of κ is relatively small in this diagnostic.

(A color version of this figure is available in the online journal.)

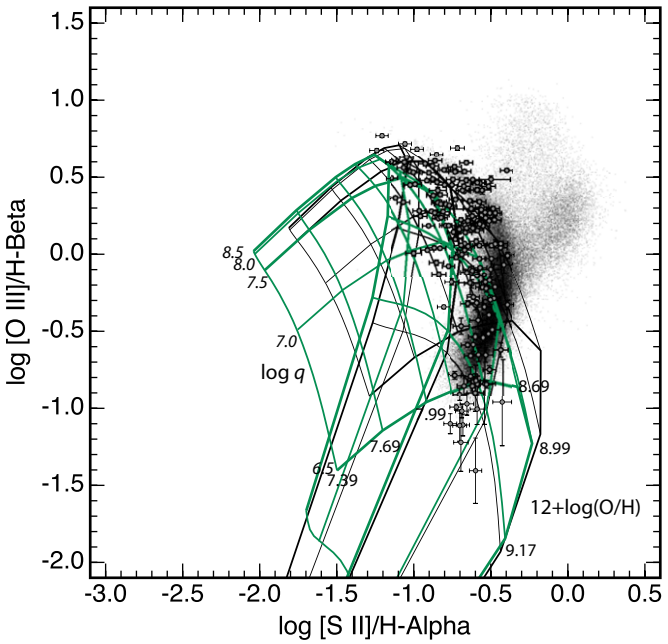

Figure 10. As in Figure 9 but for the VO87 plot of [O III] λ5007/Hβ vs. [S II] $\lambda\lambda$6717, 31/Hα. The models seem to predict slightly too weak [S II] line intensities.

(A color version of this figure is available in the online journal.)

could be understood (in part) as a result of the folding of the log(Z): log(q) surface, which ensures that H II regions having a wide range in these parameters occupy the same region of the diagnostic diagram. Dopita et al. (2006b) demonstrated that the ionization parameter, the hardness of the ionizing spectrum, and the metallicity are tightly correlated, and provided a theoretical explanation of why this fact should be the case. Both of these effects clearly play a role in making a tight H II region and starburst sequence. The fundamental difficulty with the theoretical models is that the "fold" in the surface was not the correct shape, presumably due to a combination of errors or incompatibilities in the stellar atmospheres used, issues with the atomic data used, or errors in the modeling procedure, especially in the treatment of the geometry of the H II region and in the treatment of dust absorption in the H II region. Dopita et al. (2006b) made an attempt to take into account the time evolution of the spectrum of an H II region as the stellar cluster ages and as the nebular shell expands. This analysis showed that the more recent STARBURST99 atmospheres were definitely too soft in their EUV spectra, as a consequence of the use of non-clumpy stellar winds. This analysis also showed that most extragalactic H II regions are observed when they are very young ($\lesssim$2 Myr), shortly after the absorbing placental dust cloud is dispersed, when the pressure—and hence the emissivity—in the H II region is high, and before the central stars fade in their EUV photon production rate.

The models presented here represent a great improvement over the earlier work of our group, although we should note in passing that the models of Stasińska et al. (2006) provide a rather good description of the upper envelope of the H II region-like points on these diagrams. In Figure 9, we present the VO87 plot of [O III] λ5007/Hβ versus [N II]λ6584/Hα. This figure should be compared to Figure 2 of Dopita et al. (2000), showing the improvement in the fit of the theory compared with the observations. Important contributors to this improvement are the proper treatment of the EUV absorption dust, improved atomic data, the use of spherical models, and the fact that the nebular abundance set is now fully compatible with the stellar model atmospheres.

In Figure 10, we present the VO87 plot for [O III] λ5007/Hβ versus [S II] $\lambda\lambda$6717, 31/Hα. Once again, there is a great improvement in the fit between theory and observation (cf. Figure 3 of Dopita et al. 2000). However, the [S II] lines are perhaps

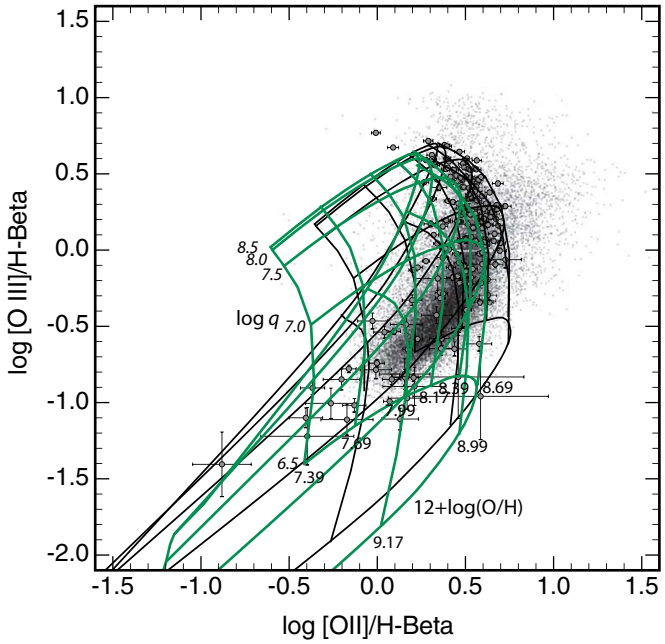

Figure 11. As in Figure 9 but for [O III] λ5007/Hβ vs. [O II]λλ3727, 9/Hβ.
(A color version of this figure is available in the online journal.)

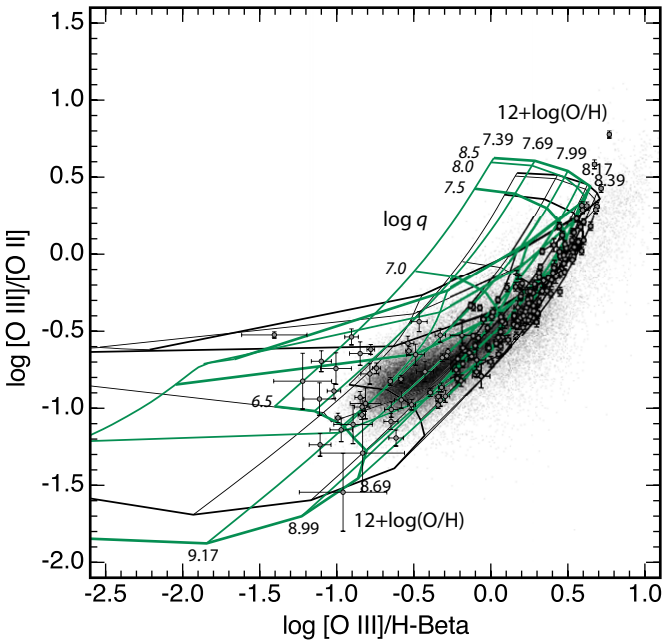

Figure 12. Excitation-sensitive ratios [O III] λ5007/[O II] λλ3727, 9 and [O III] λ5007/Hβ plotted against each other. This plot is a transposed version of one of the BPT diagnostics. Clearly, [O III] λ5007/Hβ shows a rather greater sensitivity to the chemical abundance than does [O III]λ5007/[O II]λλ3727, 9, but both ratios depend upon a mixture of both 12+log(O/H) and log q. Neither ratio can be used alone to estimate the excitation.
(A color version of this figure is available in the online journal.)

about 0.1 dex too weak. At the high abundance end, the observed sequence is best explained by the H II regions having a roughly constant log(q), between approximately 7.0–7.5. This hypothesis is confirmed in the many diagnostics presented below.

We have not attempted to provide the third diagnostic, [O I] λ6300/Hα versus [O III] λ5007/Hβ. This fact is because the [O I] line arises in a very narrow zone close to the ionization front, where shocks and non-equilibrium heating may well be important. Dopita et al. (1997) noted that shocks have a significant effect on this line ratio even when the ratio of mechanical energy to photon energy flux is as small as 10^{-3}. We therefore regard our computations of this line as much more unreliable than those of the other two lines. However, the intensity of the line is given in Table 5, if the theoretical values are required by the reader for any reason.

Closely related to the above diagnostics is that of [O III] λ5007/Hβ versus [O II]λλ3727, 9/Hβ. For completeness, this ratio is shown in Figure 11. The observational errors on the x-axis are somewhat greater because of uncertain reddening corrections.

7.2. Excitation-dependent Diagnostics

Baldwin et al. (1981) were the first to emphasize the importance of nebular excitation, measured by ratios such as [O III] λ5007/[O II] λ3727, 9, in distinguishing and separating the various modes of ionization commonly observed in nature (H II regions, planetary nebulae (PNe), power-law ionized or shock excited). These Baldwin, Phillips, & Terlevich diagnostics have since been collectively termed "BPT diagrams". Within a given class of object, such ratios are also sensitive to the ionization parameter. For H II regions, Baldwin et al. (1981) showed that [O III] λ5007/Hβ is also correlated with [O III] λ5007/[O II] λλ3727, 9, as it is separately in the case of PNe. In Figure 12, we show how well these two line ratios track each other. As it stands, this plot is not very useful. It neither effectively separates 12+log(O/H) from log q, nor does it reveal the active galactic nucleus (AGN) as a separate branch.

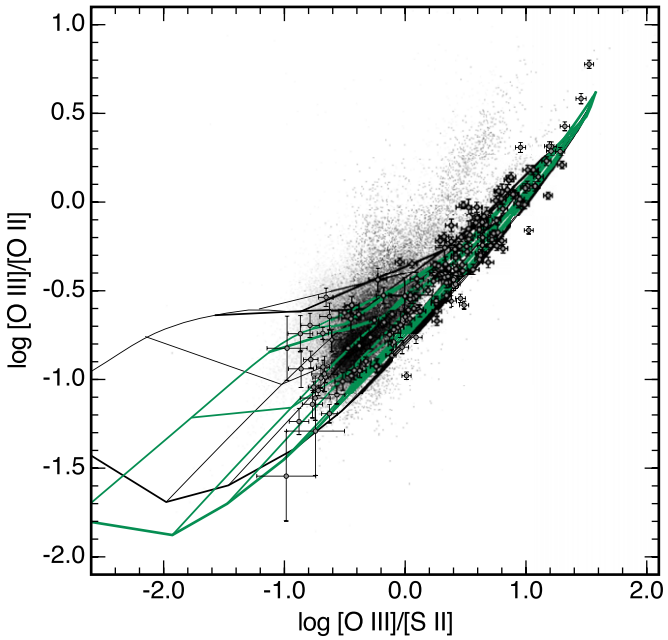

Figure 13. Excitation-sensitive ratio [O III]λ5007/[O II]λλ3727, 9 plotted against a second excitation-sensitive ratio [O III]λ5007/[S II]λ6717, 31. The two ratios show good sensitivity to the ionization parameter at abundances less than solar, and the two AGN sequences are now clearly distinguished. Due to the great degeneracy of the theoretical curves on this plot, we have not attempted to label the individual curves. Suffice it to note that the high abundance objects are located in the lower left-hand corner of the plot.
(A color version of this figure is available in the online journal.)

A better excitation-dependent diagnostic is obtained if we substitute the excitation-dependent ratio [O III] λ5007/[S II] λλ6717, 31 for [O III] λ5007/Hβ, as shown in Figure 13. Both ratios provide a similar sensitivity to ionization parameter

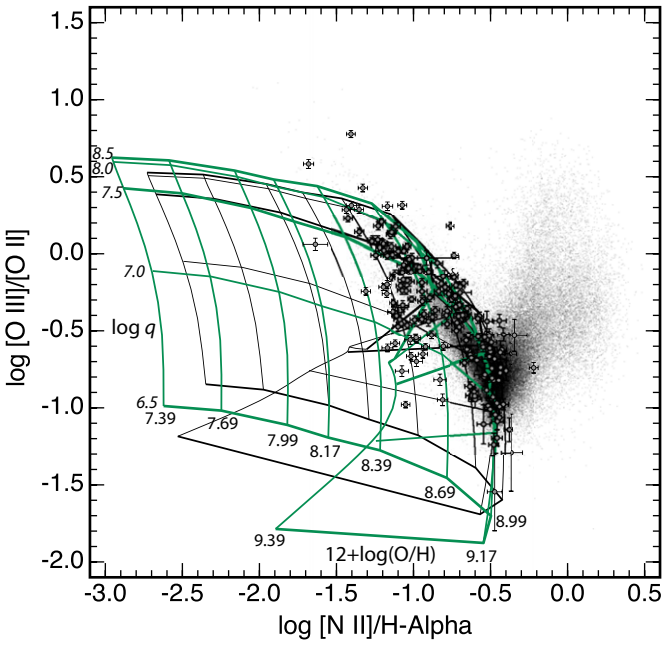

Figure 14. [O III] λ5007/[O II] λλ3727, 9 vs. [N II] λ6584/Hα. This diagnostic is one of the BPT diagnostics, with the axes transposed. Both this diagram and Figure 9 provide a clean separation of the H II region sequence from the Seyfert and LINER branches. However, this figure might prove more useful in separating the Seyfert and LINER branches than Figure 9.

(A color version of this figure is available in the online journal.)

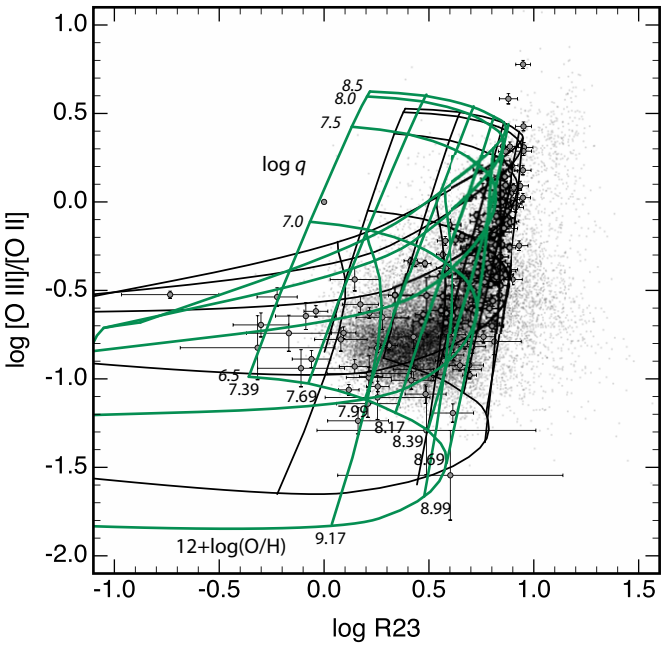

Figure 15. R_{23} ratio, [O III] λ5007/[O II] λλ3727, 9 (Pagel et al. 1979) plotted against the excitation-sensitive ([O II] λλ3727, 9 + [O III] λλ4959, 5007)/Hβ ratio. This diagram graphically illustrates the serious problems associated with any attempt to derive the chemical abundance from the R_{23} ratio alone. We strongly recommend against the use of this ratio as an abundance diagnostic.

(A color version of this figure is available in the online journal.)

at abundances less than solar, and in this abundance range the abundance sensitivity is also weak. Clearly, we can substitute [S II]λλ6717, 31 in place of [O II]λλ3727, 9, if necessary. This substitution is useful if reddening corrections are uncertain or if the nebular spectra obtained do not extend much below Hβ.

Given the similar sensitivity of both [O III] λ5007/Hβ and [O III]λ5007/[O II]λλ3727, 9 ratios to both excitation and chemical abundance, we examine the substitution of the second for the first in the Baldwin et al. (1981) and Veilleux & Osterbrock (1987) diagnostic diagram in Figure 14. This diagram is, in fact, another Baldwin et al. (1981) diagram (with transposition of the axes). Again, as in Figure 9, there is a clean separation of the AGN-excited objects from the narrow H II region sequence.

7.3. Abundance-sensitive Diagnostics

7.3.1. The R_{23} Diagnostic

It has been traditional to use the ratio of a forbidden line to a hydrogen recombination line in the quest to determine chemical abundance. However, all such ratios are two-valued in terms of abundance. As a consequence, a great deal of effort has been expended in identifying the appropriate "branch" a particular H II region lies upon in diagnostics such as the R_{23} ratio, ([O II] λλ3727, 9 + [O III] λλ4959, 5007)/Hβ (Pagel et al. 1979), or in similar ratios such as S_{23} = ([S II] λλ6717, 31 + [S III] λλ9069, 9532)/Hβ (Diaz & Pérez-Montero 2000; Oey et al. 2002).

For the R_{23} ratio, in particular, the use of both the visible forbidden line of [O III] and the UV [O II] line together mixes two regions of different H II region temperatures, and makes the maximum of this line ratio very broad in terms of abundance. This result makes the actual abundance very difficult to estimate in the region of the maximum, and it becomes critical to have a good estimate of the ionization parameter to remove the residual sensitivity of the R_{23} ratio to this parameter. This point was emphasized by McGaugh (1991).

These problems become very evident in Figure 15, in which we plot the R_{23} ratio, [O III] λ5007/[O II] λ*l*3727, 9 (Pagel et al. 1979), against the excitation-sensitive ([O II] λλ3727, 9 + [O III] λλ4959, 5007)/Hβ ratio, as was done by McGaugh (1991). First, the ratio is only weakly dependent on abundance for a broad range of abundance, $8.3 > 12+\log(O/H) > 9.0$, approximately. Second, in this range the sensitivity to the ionization parameter is as great as is the sensitivity to the abundance. Elsewhere, the ratio is two-valued, leading to the associated problems of determining whether the abundance solution lies on the low- or high-abundance branches. All these issues apply whether or not the electrons have a κ-distribution. In conclusion, therefore, we strongly recommend against use of the R_{23} ratio, ([O II] λλ3727, 9 + [O III] λλ4959, 5007)/Hβ, in attempts to determine chemical abundances, and advise observers to treat any such attempts with a great deal of caution.

7.3.2. Ratios of Strong Forbidden Lines

Unlike the R_{23} diagnostic, and others that use the ratio of a forbidden line to a hydrogen recombination line, a number of purely forbidden line ratios are known to vary monotonically with abundance, such as the [N II] λ6584/[O II] λλ3727, 29 ratio (Dopita et al. 2000), or the [Ar III]λ7135/[O III]λ5007 and the [S III]λ9069/[O III]λ5007 ratios (Stasińska 2006). The use of such pairs of forbidden line ratios to unambiguously separate the abundance and the ionization parameter was pioneered by Evans & Dopita (1985, 1986). It seems somewhat surprising that ratios such as these have since not been much more widely employed for strong line abundance diagnostics. Perhaps this fact is the result of a natural psychological pressure to include hydrogen if an attempt is being made to determine the abundance of a heavy element with respect to hydrogen.

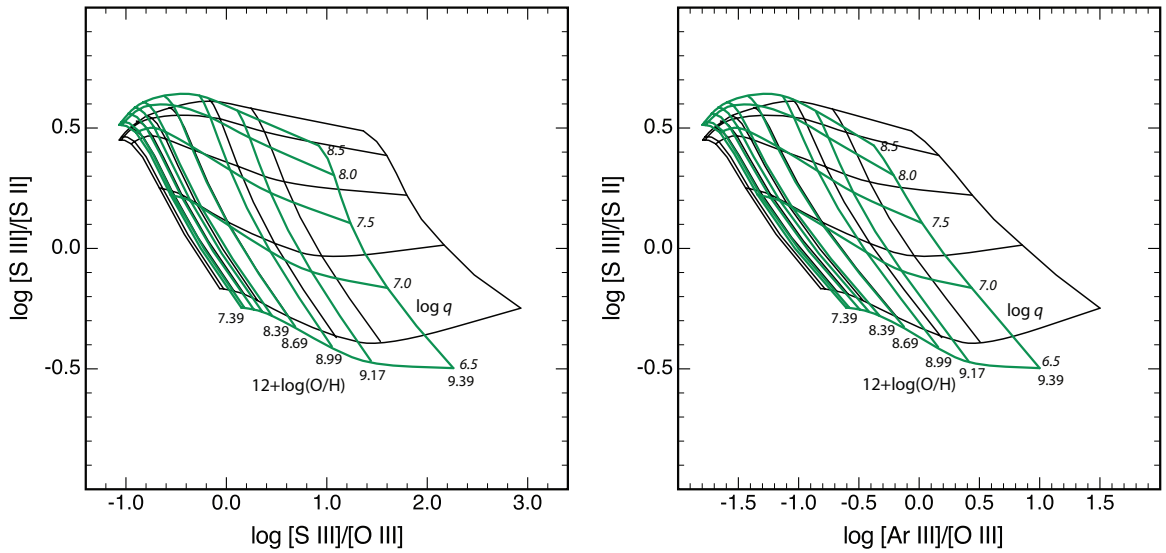

Figure 16. Stasińska (2006) excitation-sensitive [S III] λ9069/[S II] λ6717, 31 ratio plotted against the abundance-sensitive ratios. As before, the black grids correspond to $\kappa = \infty$ and the green labeled grids correspond to $\kappa = 20$. The data sets we are using do not give the [S III] λ9069 line fluxes, and so cannot be plotted on these diagrams. Note that the behavior of both abundance indicators is similar, as both are relatively insensitive to abundance below $12 + \log(O/H) < 8.0$ and show considerable sensitivity to the ionization parameter.

(A color version of this figure is available in the online journal.)

In Figure 16, we show the two ratios used by Stasińska (2006). Here, we have used the excitation-sensitive [S III]λ9069/[S II]λ6717, 31 ratio as the prime ionization parameter diagnostic. Both abundance indicators are similar, being relatively insensitive to abundances below 12+log(O/H) < 8.0 and showing considerable sensitivity to ionization parameter. The data sets we are using do not have the [S III]λ9069 line fluxes, and so cannot be plotted on these diagrams. In addition, the excitation-sensitive [O III]λ5007/[S II]λ6717, 31 ratio cannot be substituted on the *y*-axis, as the ratios then become degenerate.

As pointed out by Stasińska (2006), these ratios work because they (indirectly) measure the electron temperature in the high-ionization zone of the H II region. At high abundances, the temperature of this zone changes rapidly with abundance, giving the observed sensitivity at the high abundance end. However, at the low-abundance end of the scale, the temperature sensitivity to abundance is much weaker.

7.3.3. [N II]/[O II] as an Abundance Diagnostic

Dopita et al. (2000) separated the effects of abundance and ionization parameter by using [N II] λ6584/[O II] λλ3727, 29 as the prime abundance diagnostic and using the excitation-sensitive [O III]λ5007/[O II]λλ3727, 9 ratio as the prime ionization parameter diagnostic. Our re-computation of this diagnostic is shown in Figure 17. The [N II] λ6584/[O II] λλ3727, 29 ratio is particularly sensitive to abundance for two reasons. First, nitrogen has a large secondary component of nucleosynthesis at high abundance; see Figure 3. This fact ensures an increase of [N II]/[O II]. Second, the nebular electron temperature falls systematically as the abundance increases. This fact ensures that collisional excitations of the [O II]λλ3727, 9 lines are quenched at the high abundance end of the scale.

Several points are to be noted. First, the effect of the κ-distribution on the implied chemical composition is small, but nonetheless significant. In general, the κ-distribution leads to systematically higher derived chemical abundances. Likewise, the κ-distribution tends to systematically decrease the derived ionization parameters. The most significant difference occurs

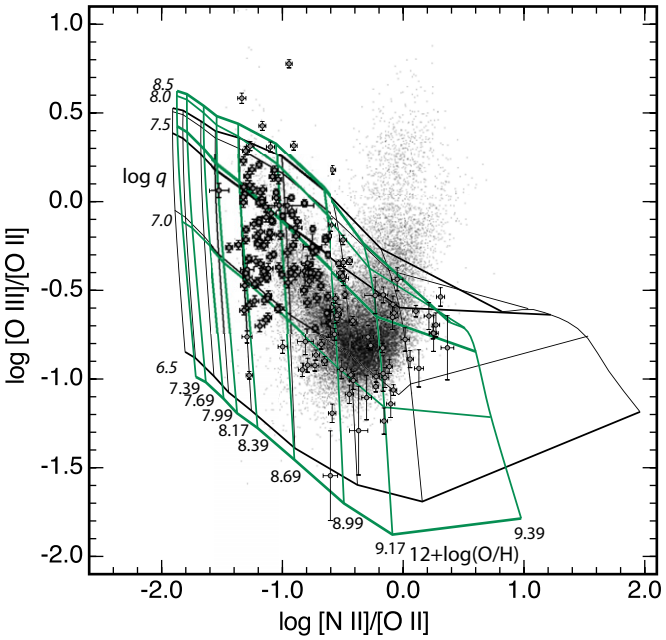

Figure 17. Dopita et al. (2000) diagnostic diagram. This diagram clearly separates the abundance from the ionization parameter. Note that the SDSS galaxies and the van Zee et al. (1998) sample of H II regions have a relatively restricted range of abundance parameters. Also, the AGN sequence is quite distinct in this diagnostic.

(A color version of this figure is available in the online journal.)

in the high-q, low-Z regime. Second, the vertical scatter of the observational points on this figure can be ascribed to intrinsic variability in $\log q$ between different H II regions. Most of the van Zee et al. (1998) H II regions have $\log q$ in the range 7.0–7.5, with the high-q outliers tending to be associated with low-abundance H II regions. Third, the SDSS galaxies display a systematically smaller abundance spread than the van Zee et al. (1998) sample, consistent with the fact that the SDSS spectra are heavily weighted toward the central regions of galaxies, while most of the van Zee et al. (1998) H II regions are located in

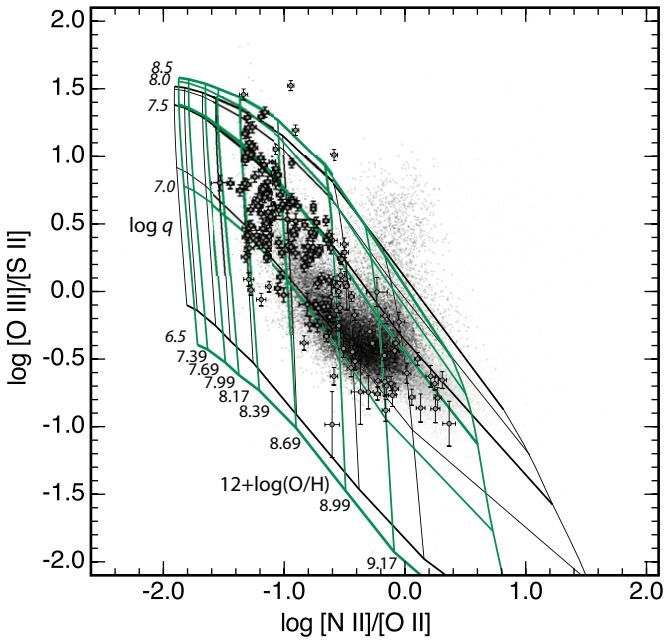

Figure 18. As in Figure 17, but substituting [O III]λ5007/[S II]λ6717, 31 in the place of [O III]λ5007/[O II]λλ3727, 9. The [O III]/[S II] ratio is more sensitive to abundance, but some of the scatter is reduced because the [O III]/[S II] ratio is much less sensitive to reddening corrections than the [O III]/[O II] ratio. The ionization parameter is more closely confined to $7.6 \gtrsim \log(q) \gtrsim 6.9$. The two grids agree closely on the abundance of the H II regions.

(A color version of this figure is available in the online journal.)

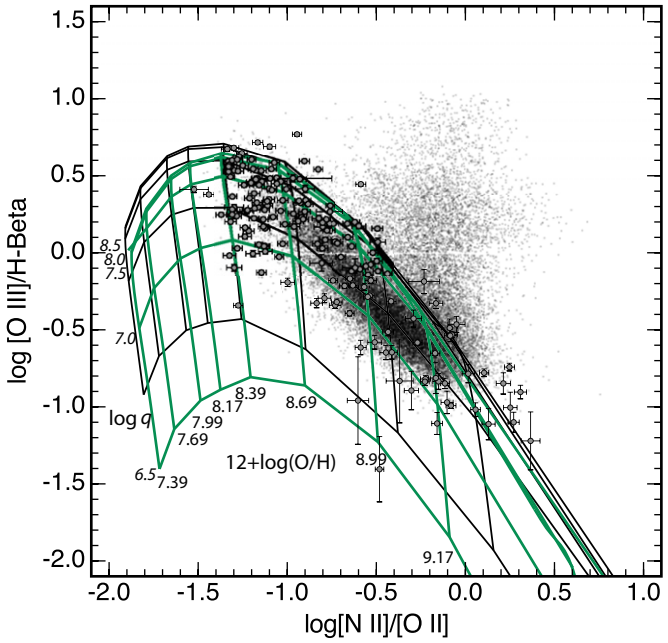

Figure 19. As in Figure 17, above, but substituting [O III]λ5007/Hβ in the place of [O III]λ5007/[O II]λλ3727, 9. This diagnostic is not so useful for determining $\log(q)$, but the sharp upper boundary of the theoretical models suggests that this diagram is very useful for distinguishing AGNs and transitional types from normal star-forming galaxies.

(A color version of this figure is available in the online journal.)

the spiral arms, which have lower oxygen abundance due to the presence of galactic abundance gradients. A few of the van Zee et al. (1998) H II regions have extremely high abundances. These H II regions are located in very luminous disk galaxies such as NGC 1068, NGC 1637, and NGC 3184. Lastly, the SDSS galaxies clearly show the AGN branches emerging in the vertical

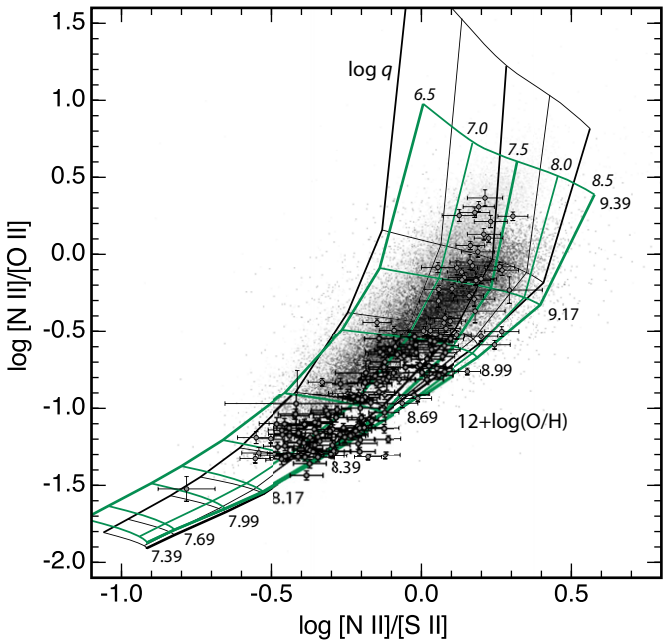

Figure 20. [N II]/[S II] and [N II]/[O II] compared as abundance diagnostics. Clearly, both are sensitive to abundance, but for [N II]/[S II] the sensitivity is weaker, and there is a greater sensitivity to $\log(q)$. The AGN sequence is not distinguished in this diagnostic diagram.

(A color version of this figure is available in the online journal.)

direction from the main cloud of galaxies. This fact implies that most of the AGNs in the local universe are associated with super-solar chemical abundances, $12 + \log(\mathrm{O/H}) \gtrsim 9.0$.

We had already demonstrated in Figure 13, above, that either [O III]λ5007/[O II]λλ3727, 9 or [O III]λ5007/[S II]λ6717, 31 can provide good excitation diagnostics. Figure 18 shows the effect of making this substitution in the Dopita et al. (2000) diagnostic, which we have just discussed. The abundances implied by both diagnostics agree closely, as they should, since only the [N II] λ6584/[O II] λλ3727, 29 is sensitive to abundance. However, the scatter in the inferred $\log(q)$ is reduced in Figure 18. This result is almost certainly because the reddening corrections and their associated errors are much smaller for the [O III]/[S II] ratio than for the [O III]/[O II] ratio. It is now evident that the observed range of ionization parameter for either the spiral arm H II regions or the SDSS nuclear spectra is rather restricted; most objects are located in the narrow band $6.9 \lesssim \log(q) \lesssim 7.6$.

If we try to use the excitation-sensitive [O III]λ5007/Hβ on the y-axis, we obtain the diagnostic diagram in Figure 19. This diagram is degenerate in terms of the ionization parameter over a wide range for higher values of $\log(q)$. This diagram is probably better suited to separate the AGN galaxies from the normal star-forming galaxies, despite the fact that it distinguishes between the LINER and Seyfert sequences rather poorly.

7.3.4. [N II]/[S II] as an Abundance Diagnostic

Given that [N II] λ6584/[O II] λλ3727, 29 is the ratio of an element formed in intermediate mass stars to a standard α-process element, it is reasonable to ask whether another α-process element could be substituted for oxygen. An obvious candidate to use is [S II]λ6717, 31. In Figure 20, we compare [N II]λ6584/[S II]λ6717, 31 to the [N II] λ6584/[O II] λλ3727, 29 ratio. Both ratios are sensitive to abundance, except that [N II]λ6584/[S II]λ6717, 31 is more sensitive to the ionization parameter, which is a consequence of the mis-match of the

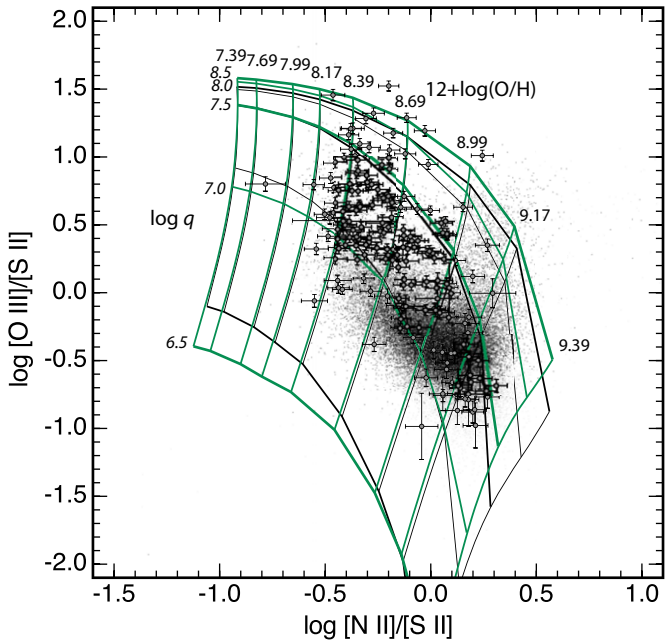

Figure 21. [O III]/[S II] vs. [N II]/[S II]. This new diagnostic diagram is valuable for several reasons. First, it provides an excellent separation of log(q) and 12+log(O/H). Second, the reddening corrections are simple to make. Third, only a limited spectral coverage is required.

(A color version of this figure is available in the online journal.)

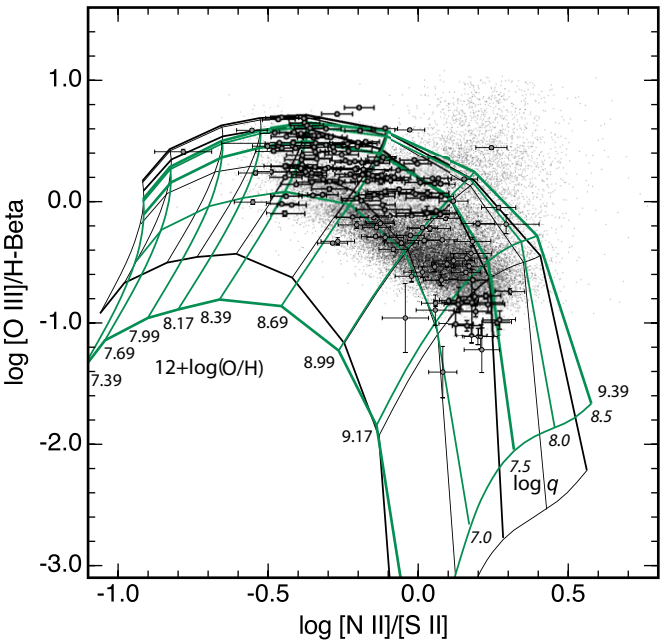

Figure 22. [O III]/Hβ vs. [N II]/[S II]. This new diagnostic diagram is useful for the same reasons as Figure 21, except perhaps at the high ionization parameter and low abundance limit.

(A color version of this figure is available in the online journal.)

ionization potential of S II as compared to either N II or O II. In addition, the sensitivity of the ratio to abundance is less, because the ratio of collisional excitation rates of [N II] and [S II] is a very weak function of nebular temperature.

The great advantage in the use of [N II]/[S II] as an abundance diagnostic is that reddening corrections are negligible, facilitating an accurate determination of the line ratio. To minimize the reddening corrections in the determination of the excitation, an obvious choice is to use the [O III]/[S II] ratio, since the S II line is close to Hα, the O III line is close to Hβ, and the intrinsic Balmer decrement is well defined. In this context, we should note that our models provide a systematically higher Hα/Hβ ratio than the standard Case B recombination value, as can be seen in Table 5. This fact is a result of the important contribution of collisional excitation from the metastable $2^1S_{1/2}$ level to the Hα line flux, since there is a large resonance just above threshold in the collisional cross section of this line.

Figure 21 shows [O III]/[S II] versus [N II]/[S II]. This new diagnostic is very useful, since it provides an excellent discrimination between 12+log(O/H) and log(q) over the full range of both these parameters. Comparing with Figure 18, it is clear that observational data provide very similar solutions for both of these parameters. In addition, spectra of limited wavelength coverage and poor spectrophotometric calibration can be used to provide robust solutions for both 12+log(O/H) and log(q). Finally, for this diagnostic, it hardly matters whether the κ-distribution applies or not, since both theoretical grids overlap almost perfectly.

A useful diagnostic is also obtained if we substitute [O III]/Hβ for [O III]/[S II] as our excitation-dependent diagnostic ratio. This result is shown in Figure 22. This diagnostic suffers a little from the issues of Figure 19 in that it is not very capable of distinguishing q at the high ionization parameter limit. This tendency is more marked at the low-abundance end. However, the AGN sequence is well distinguished, and like Figure 21, it has the advantage that spectra of limited wavelength coverage and poor spectrophotometric calibration can be used to provide a good solution.

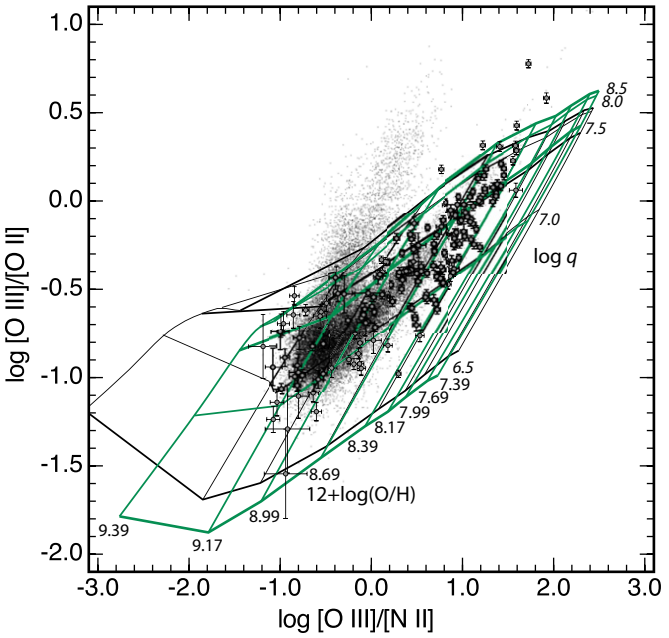

Figure 23. Alloin et al. (1979) abundance-sensitive diagnostic [O III]/[O II] plotted against the excitation-dependent [O III]/[N II] ratio. Both ratios are also sensitive to log q, but provide sufficient sensitivity to both abundance and ionization parameter to make this diagnostic diagram useful. In addition, the AGN branch is quite distinct.

(A color version of this figure is available in the online journal.)

7.3.5. The Alloin et al. (1979) Abundance Diagnostic

Alloin et al. (1979) suggested that the ratio [O III]/[N II] could provide a good abundance diagnostic since these authors demonstrated a good correlation between this ratio and the

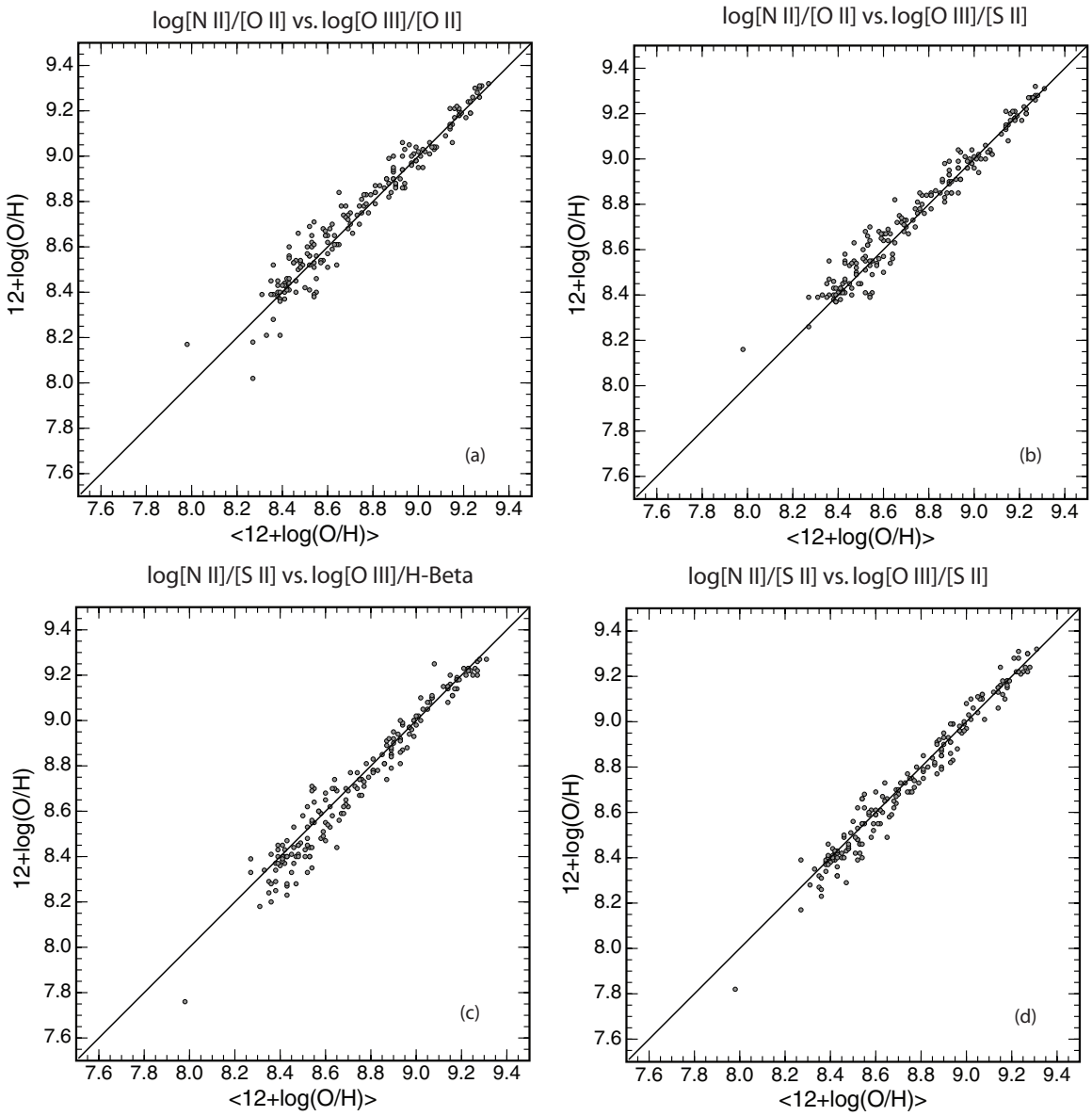

Figure 24. Chemical abundances derived for the van Zee et al. (1998) H II regions using each of the four diagnostics given on the label, plotted against the average of all four.

measured electron temperature. In turn, the electron temperature is inversely correlated with chemical composition (cf. Figure 4, above). However, as we have amply demonstrated above, no one ratio provides either a clean abundance diagnostic or a clean ionization parameter diagnostic. All are sensitive to both parameters. Figure 23 brings out this point. Here, we have plotted [O III]/[O II] against the excitation-dependent [O III]/[N II] ratio. This figure also provides a clean separation of the abundance from the ionization parameter over the full range of these parameters, and shows very little sensitivity to the value of κ.

8. APPLYING THE ABUNDANCE DIAGNOSTICS

8.1. Self-consistency

Before applying the new diagnostics, it is mandatory to check them for self-consistency. For this purpose, we have selected the four best diagnostics on the grounds that they should adequately separate the two parameters, log(q) and 12+log(O/H), and be sensitive to these over the full range of both parameters. Bearing in mind that many of the diagnostics are not truly independent, since they employ the same line ratios in at least one axis, we have selected a subset of four, two based upon [N II]/[O II] and two based upon [N II]/[S II]:

1. [N II]/[O II] versus [O III]/[O II],
2. [N II]/[O II] versus [O III]/[S II],
3. [N II]/[S II] versus [O III]/Hβ, and
4. [N II]/[S II] versus [O III]/[S II].

For the observational test set, we have used the homogeneous van Zee et al. (1998) observations, which cover a wide abundance range of H II regions in several galaxies. For each of these, we have graphically solved for the implied oxygen abundance (to the nearest 0.01 dex) and for the ionization parameter (to the nearest 0.1 dex) using our four diagnostics. A value of $\kappa = 20$ was assumed, on the basis of the discussion in Section 5. We then formed a global average for each of the parameters using all four diagnostics. The results are shown in Figure 24 for the chemical abundances and in Figure 25 for the ionization parameters.

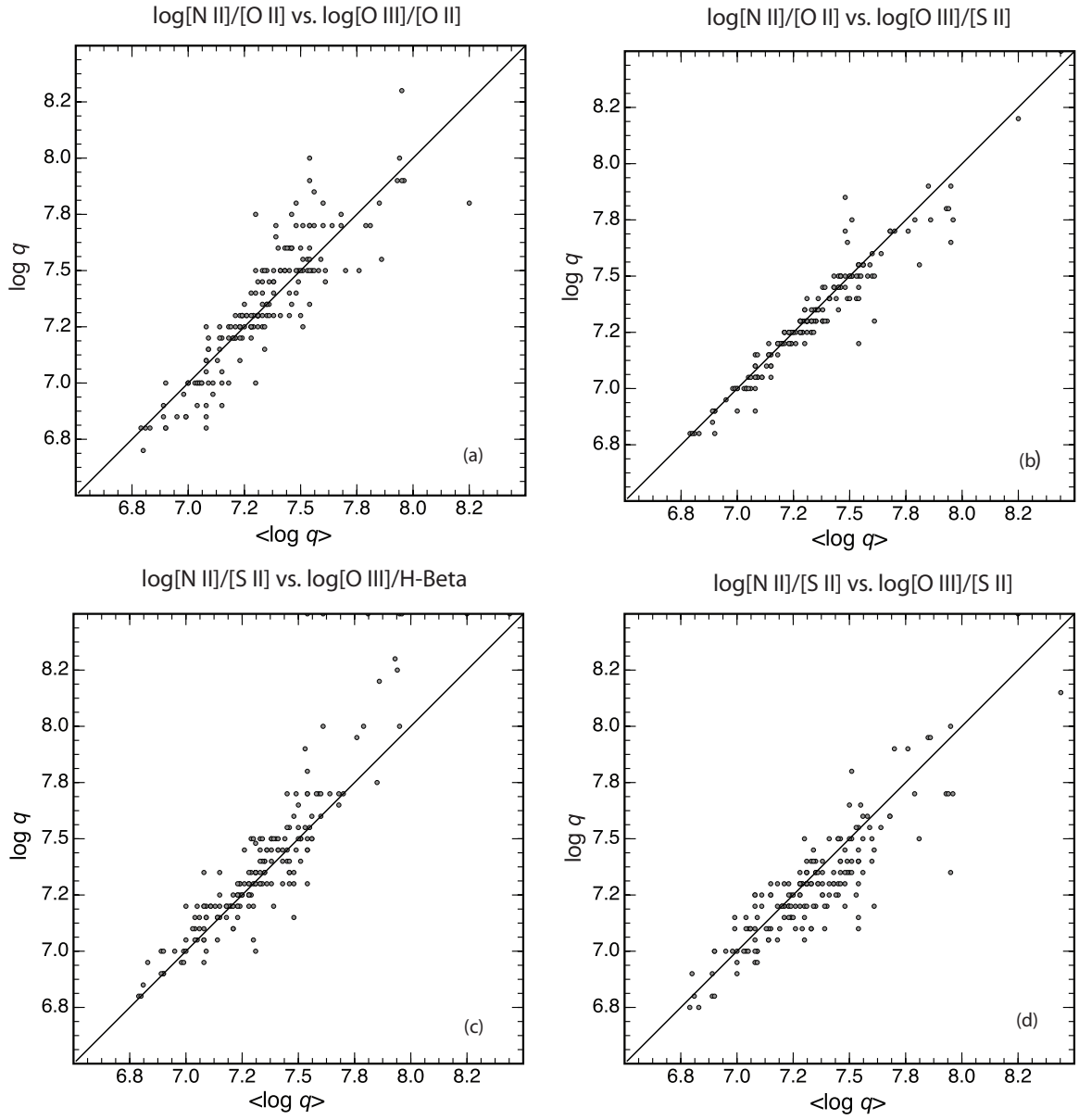

Figure 25. As in Figure 24, but for the derived ionization parameter.

It is clear that all four methods are in remarkably close agreement with each other. For those abundance diagnostics involving [O II], the scatter is somewhat larger, presumably reflecting increased photometric and reddening correction errors. As expected, the [N II]/[S II] versus [O III]/[S II] diagnostic gives the smallest scatter. There appears to be little or no systematic difference in derived abundance as a function of abundance for any of the diagnostics.

For the ionization parameter, [N II]/[O II] versus [O III]/[S II] gives the smallest scatter. For [N II]/[O II] versus [O III]/[O II] a small systematic trend toward higher derived log(q) at higher q is apparent. [N II]/[S II] versus [O III]/[S II] gives the greatest scatter in derived log(q). However, these effects are small, and the global solution using all four diagnostics appears to be robust.

8.2. Comparison with Kewley & Dopita (2002)

Given that the Kewley & Dopita (2002) work was based upon an earlier version of the MAPPINGS code, it is interesting to see how our new abundance diagnostics compare with that earlier work. The main changes in the code that have occurred in the 11 yr since are:

1. a proper match of the stellar and nebular abundances,
2. use of the Grevesse et al. (2010) revised abundance set and new CN abundance variations,
3. inclusion of the effects of radiation pressure,
4. use of spherical geometry rather than plane parallel geometry,
5. improved atomic data (as described above), and
6. inclusion of the possibility of κ-distributed electrons.

Again, we have used the homogeneous van Zee et al. (1998) observations to facilitate this comparison, reducing the data with the procedure described in Kewley & Dopita (2002). This procedure provides four abundance diagnostics based on, respectively, the R_{23} calibration, the [N II]/[O II] versus [O III]/[O II] diagnostic, the [N II]/[S II] versus [O III]/[O II]

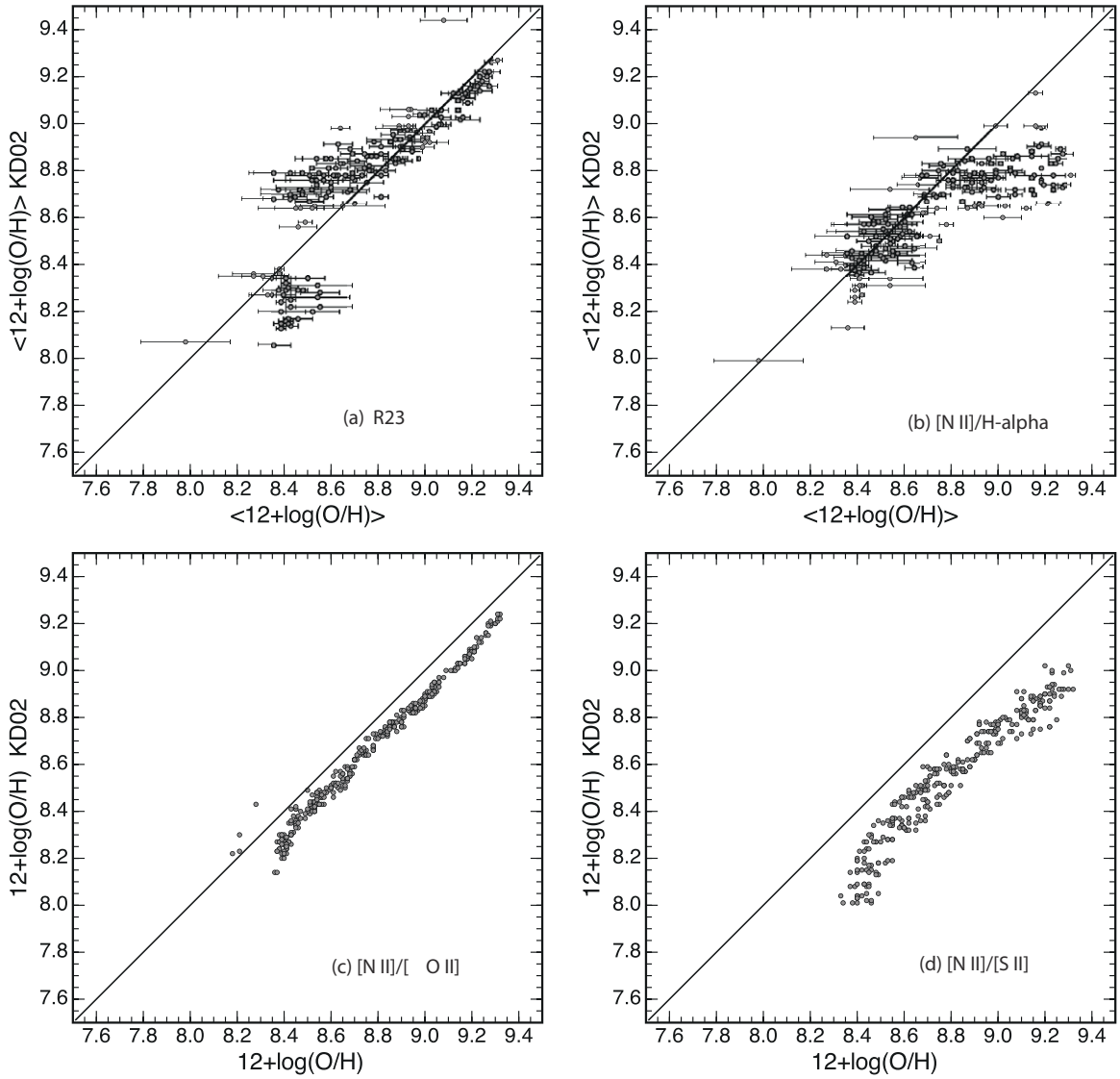

Figure 26. Abundances derived from the van Zee et al. (1998) H II regions using the Kewley & Dopita (2002) abundance diagnostics, compared with those of this paper. In panels (a) and (b), we compare the R_{23} method and the [N II]/Hα method with the mean of our abundance diagnostics. The error bars show the internal rms dispersion for our abundance estimates. In panels (c) and (d), we use the [N II]/[O II] vs. [O III]/[O II] and the [N II]/[S II] vs. [O III]/[O II] diagnostics from the Kewley & Dopita (2002) paper, compared with these same diagnostics from this paper.

diagnostic, and the [N II]/Hα ratio. The results are shown in Figure 26.

The correlation between our abundances and the Kewley & Dopita (2002) R_{23} abundances is good at the high abundance end. However, the scatter is large in the region $8.2 \lesssim 12 + \log(\mathrm{O/H}) \lesssim 8.7$, where the R_{23} indicator is almost insensitive to O/H. The [N II]/Hα method produces large scatter, with a systematic offset at the high abundance limit. As expected, the [N II]/[O II] versus [O III]/[O II] diagnostics agree very well with one another. The systematic offset can be largely ascribed to the re-calibration of the N/O abundance with respect to O/H, which provides both an offset and the curvature seen at low abundance, and the change in the stellar EUV spectra. However, the [N II]/[S II] versus [O III]/[O II] diagnostic shows both a large (~0.3 dex) offset and marked curvature.

The average of all four Kewley & Dopita (2002) diagnostics is given in Figure 27. The overall correlation is good, and this result implies that previous results on the chemical composition of galaxies based on the Kewley & Dopita (2002) diagnostics do not need revision except perhaps at the low- and high-abundance extremes.

8.3. Comparison with van Zee et al. (1998)

In their paper, van Zee et al. (1998) used a hybrid technique to determine abundances based upon both strong lines and a calibration of the excitation with the T_e measured for a small subset of their sample. In essence, therefore, this procedure is essentially a T_e-based calibration, similar to those used by Pilyugin and his collaborators (Pilyugin 2001a, 2001b; Pilyugin & Thuan 2005; Pilyugin & Mattsson 2011; Pilyugin et al. 2012). In Figure 28, we show the correlation between the van Zee et al. (1998) abundances and those derived in this paper. Note that although the correlation is very good, there is a small systematic offset between the two abundances in the same sense as is usually found for strong line methods calibrated using photoionization models compared with methods based on T_e (see the discussion in the Introduction).

Table 7
Line Ratio Diagnostics Used with the pyqz Python Module v0.2 and Their Associated Regions of Validity in $\log Z = 12 + \log(O/H)$ and $\log q$ Space

Line Ratios	$\kappa = 10$		$\kappa = 20$		$\kappa = 50$		$\kappa = \infty$	
	$\log Z$	$\log q$	$\log Z$	$\log q$	$\log Z$	$\log q$	$\log Z$	$\log q$
[N II]/[S II] vs. [O III]/[S II]	7.39–9.39	6.5–8.5	7.39–9.39	6.5–8.5	7.39–9.39	6.5–8.5	7.39–9.39	6.5–8.5
[N II]/[S II] vs. [O III]/Hβ	7.39–9.39	6.5–8.5	7.39–9.39	6.5–8.5	7.39–9.39	6.5–8.25	7.39–9.39	6.5–8.5
[N II]/[S II] vs. [O III]/[O II]	7.39–9.39	6.5–8.5	7.39–9.39	6.5–8.5	7.39–9.39	6.5–8.5	7.39–8.99	6.5–8.5
[N II]/[O II] vs. [O III]/[S II]	7.39–9.39	6.5–8.5	7.39–9.39	6.5–8.5	7.39–9.39	6.5–8.5	7.39–9.39	6.5–8.5
[N II]/[O II] vs. [O III]/Hβ	7.39–9.39	6.5–7.5	7.39–9.39	6.5–7.5	7.39–9.39	6.5–7.5	7.39–9.39	6.5–7.5
[N II]/[O II] vs. [O III]/[O II]	7.39–9.39	6.5–8.25	7.39–9.39	6.5–8.0	7.39–9.39	6.5–7.75	7.39–9.39	6.5–7.75
[N II]/Hα vs. [O III]/Hβ	7.39–8.69	6.5–8.5	7.39–8.39	6.5–8.5	7.39–8.39	6.5–8.25	7.39–8.39	6.5–8.5
[N II]/Hα vs. [O III]/[O II]	7.39–8.69	6.5–8.5	7.39–8.39	6.5–8.5	7.39–8.17	6.5–8.25	7.39–7.99	6.5–8.5

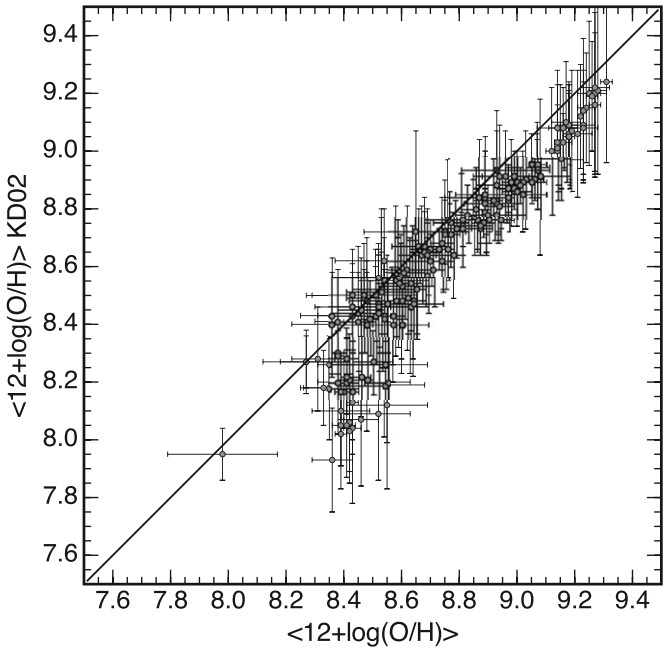

Figure 27. Mean of the Kewley & Dopita (2002) diagnostics plotted against the mean of the diagnostics used in this paper. The error bars are the rms scatter of the four diagnostics used to create the mean in each case. The systematic offset can be largely ascribed to the offset of the [N II]/[O II] and [N II]/[S II] diagnostics.

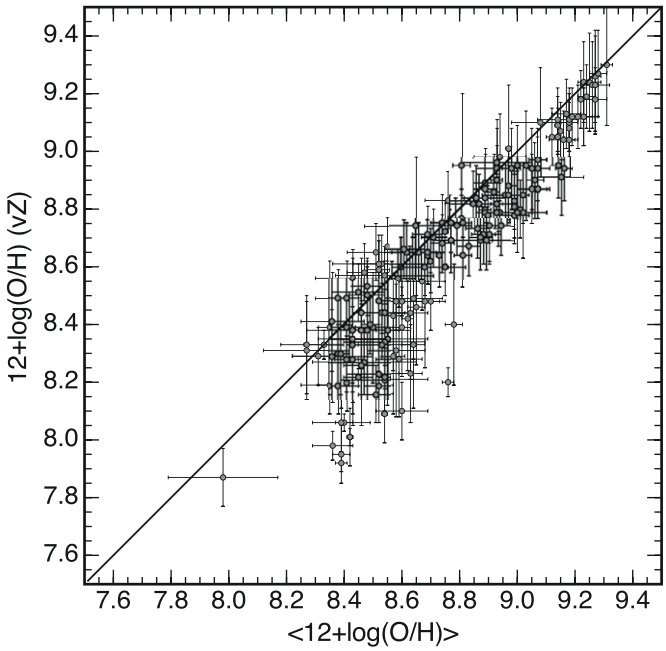

Figure 28. Abundances derived by van Zee et al. (1998) for their H II regions compared with the abundances derived here. Note the close similarity with Figure 27. Here, the systematic offset of ~0.2 dex can be understood as another manifestation of the systematic offset always found between strong-line and T_e-based abundance determinations (López-Sánchez et al. 2012).

van Zee et al. (1998) also compared their data with abundances determined by two strong line methods based upon the R_{23} ratio: that of Zaritsky et al. (1994) and that of Edmunds & Pagel (1984). The comparison of these two methods with our abundances is shown in Figure 29. Note that the Zaritsky et al. (1994) method is applicable only to the high abundance branch, which is why the scatter increases below $12 + \log(O/H) \sim 8.7$. Otherwise, this method agrees rather closely with our results. As previously found in Kewley & Dopita (2002), the Edmunds & Pagel (1984) method is subject to large systematic errors.

8.4. An Automated Technique to Derive Abundances

In this paper, we have presented a grid of models covering a wide range of abundance and ionization parameters typical of H II regions in galaxies. However, given an observed set of ratios, we need to implement a two-dimensional interpolation routine to *read* the diagnostic line ratio grid between the nodes actually computed. For this purpose, we have implemented a dedicated *Python* module to perform this task automatically—the `pyqz` module. This module relies on the `griddata` function in the `scipy.interpolate` module to perform a two-dimensional fit to a given diagnostic grid. The `griddata` routine allows either a linear or piecewise cubic spline fit to an *N*-dimensional unstructured data set. We refer the reader to the *Scipy Reference Guide* for more information on the `griddata` function.[5]

As discussed in Section 7, several diagnostic grids allow a clear separation of both $\log q$ and 12+log(O/H). In Figures 30 and 31, we use our `pyqz` module to test how well these different grids can be interpolated to recover the value of $\log q$ or 12+log(O/H), respectively. Each row corresponds to a different diagnostic grid labeled accordingly. In the left and middle columns, we show the result of the interpolation performed using the linear or piecewise cubic approach. In the right column, we show the difference, in %, between the two different interpolation results. The grids in this case are computed for $\kappa = 20$. The error maps in Figures 30 and 31 do not represent absolute error on the interpolation results. Nevertheless, they indicate how well a given grid can be read. In most cases, the

[5] The information page for the `griddata` function is located at http://docs.scipy.org/doc/scipy/reference/generated/scipy.interpolate.griddata.html.

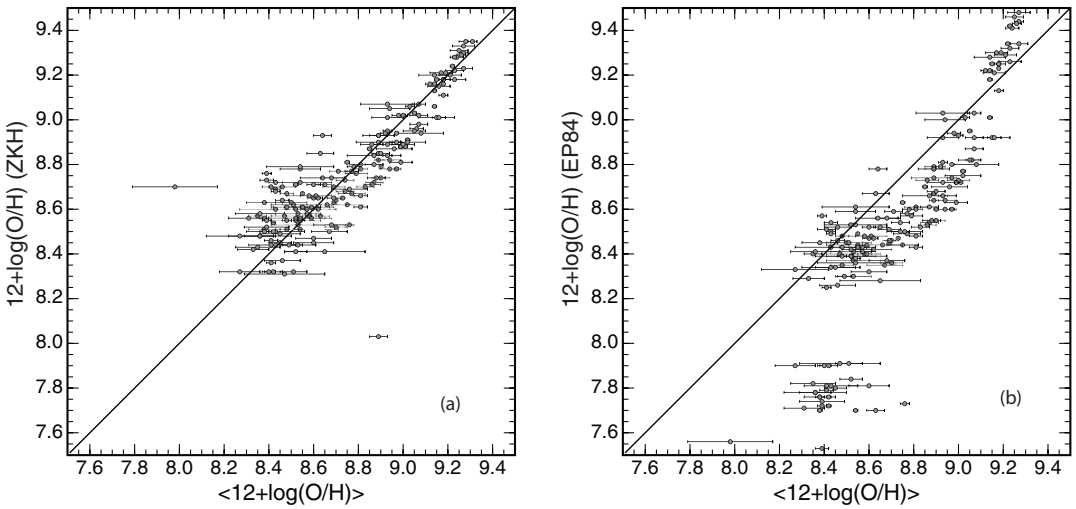

Figure 29. Abundances derived here for the Zaritsky et al. (1994) and of Edmunds & Pagel (1984) H II regions compared with those derived from the methods of van Zee et al. (1998). Both the Zaritsky et al. (1994) and of Edmunds & Pagel (1984) techniques are R_{23} techniques, but the Zaritsky et al. (1994) method is applicable only to the high abundance branch, which is why the scatter increases below $12 + \log(\mathrm{O/H}) \sim 8.7$. The Edmunds & Pagel (1984) method is clearly subject to large systematic errors.

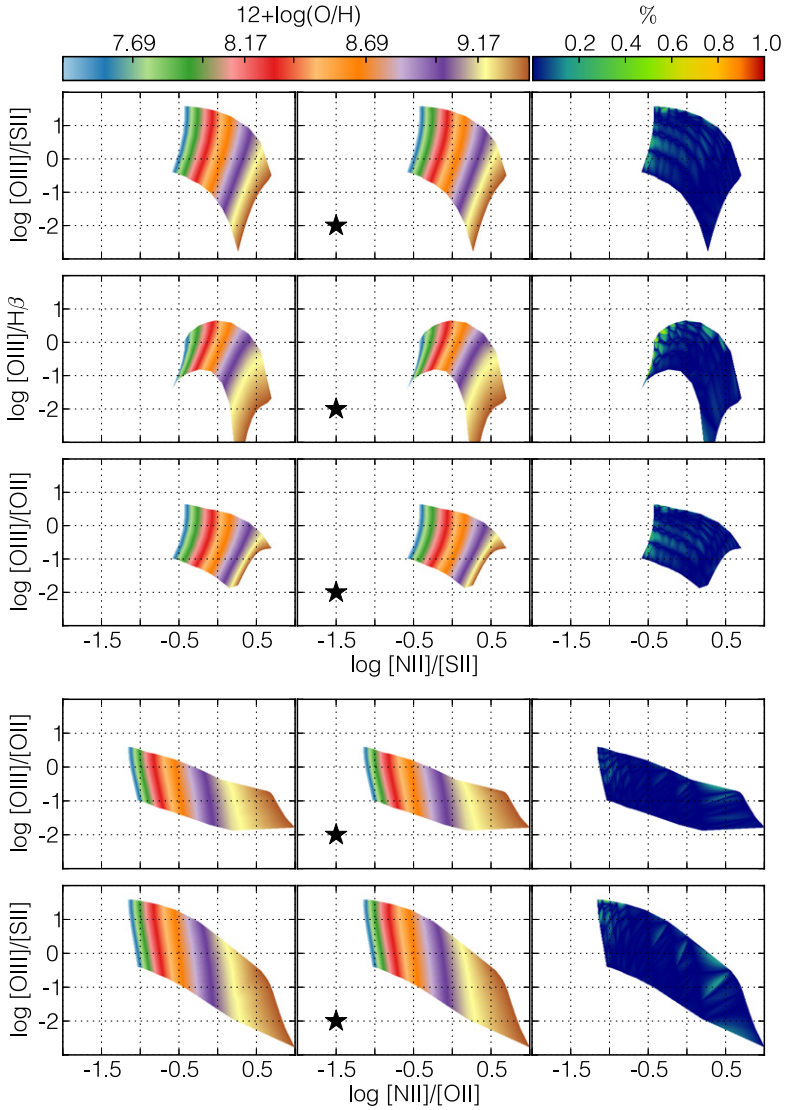

Figure 30. Side-by-side comparison between a linear and piecewise cubic interpolation of different diagnostic grids that allow for unambiguous reading of the log(O/H) value. The third column shows the difference in % between the two different interpolation methods, and is indicative of how accurately a given diagnostic grid can be read. These grids are for $\kappa = 20$.

(A color version of this figure is available in the online journal.)

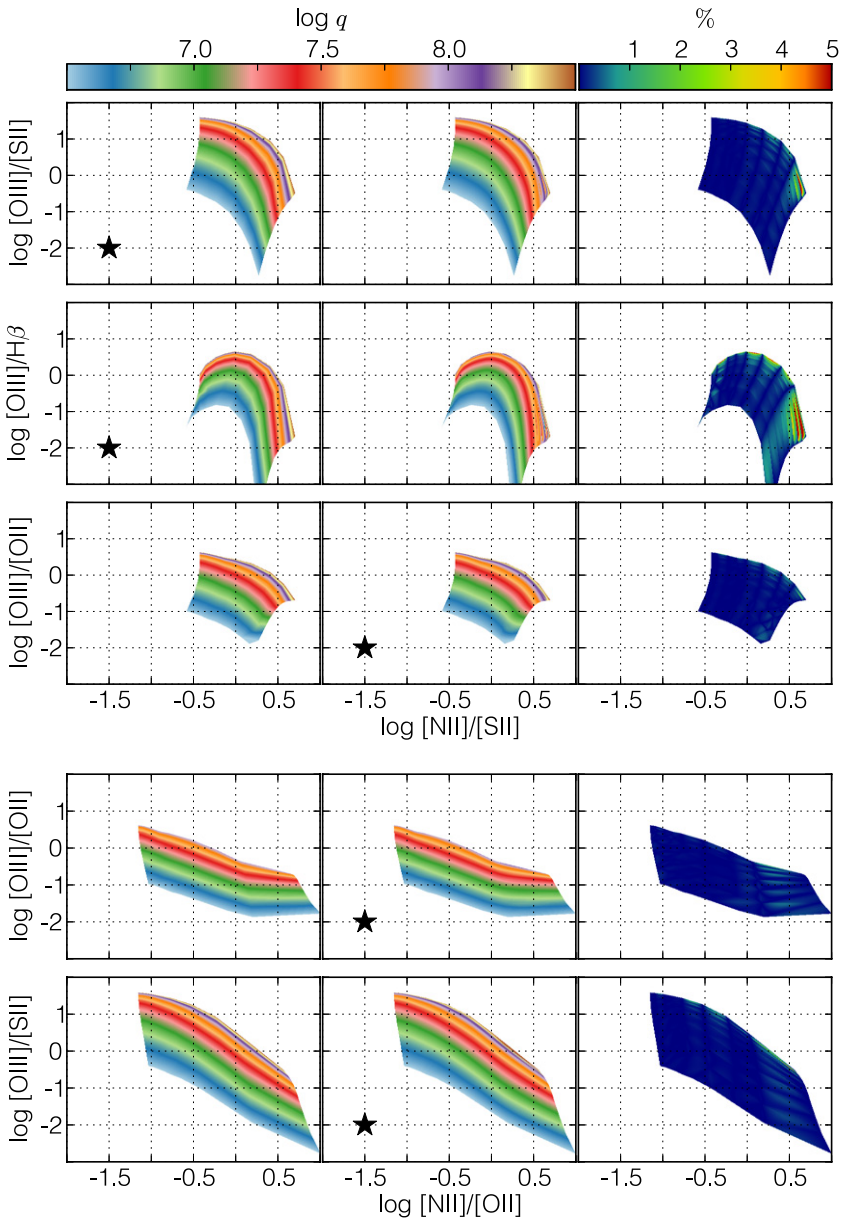

Figure 31. As in Figure 30, but for the ionization parameter log(q).
(A color version of this figure is available in the online journal.)

difference between the two interpolation methods is lower than 5%. These grids provide consistent results between the two different interpolation methods, with errors below 1% for most of the interpolation region.

For both the log q and 12+log(O/H) grids, we mark with a black star the interpolation method (linear or piecewise cubic) that provides the smoothest result based on a visual comparison of the two different interpolated grids. The absolute grid error associated with the best interpolation method can be expected to be smaller than the error map provided in the right column, which can be used as an upper estimate of the uncertainty associated with reading a given diagnostic grid. We note that the error associated with reading the grid is much smaller than errors associated with the computation of the grid itself, and observational errors affecting line ratios.

Our `pyqz` Python module (v0.4) is made freely available for the community to use under the GNU General Public License, and can be downloaded from the Australian National University Data Commons online repository (doi:10.4225/13/516366F6F24ED). This module allows observers to interpolate within any of the line ratio grids listed in Table 7 for $\kappa \in [10, 20, 50, \infty]$. With any given set of observed line ratios, the module returns the corresponding log q and 12+log(O/H) values for the chosen value of κ if the observed ratios lie within a *readable* region of the grid (with no wrapping present). The specific readable regions, for all diagnostic grids and κ, are listed in Table 7.

8.5. Implications of κ for T_e-based Abundance Diagnostics

In a future paper, we propose to examine in more detail the implications of κ-distributed electrons on abundances derived by T_e methods. However, here we will give an outline explanation of how κ could help to address the long-standing discrepancy between the abundance scales defined by strong line techniques and those defined by the T_e method.

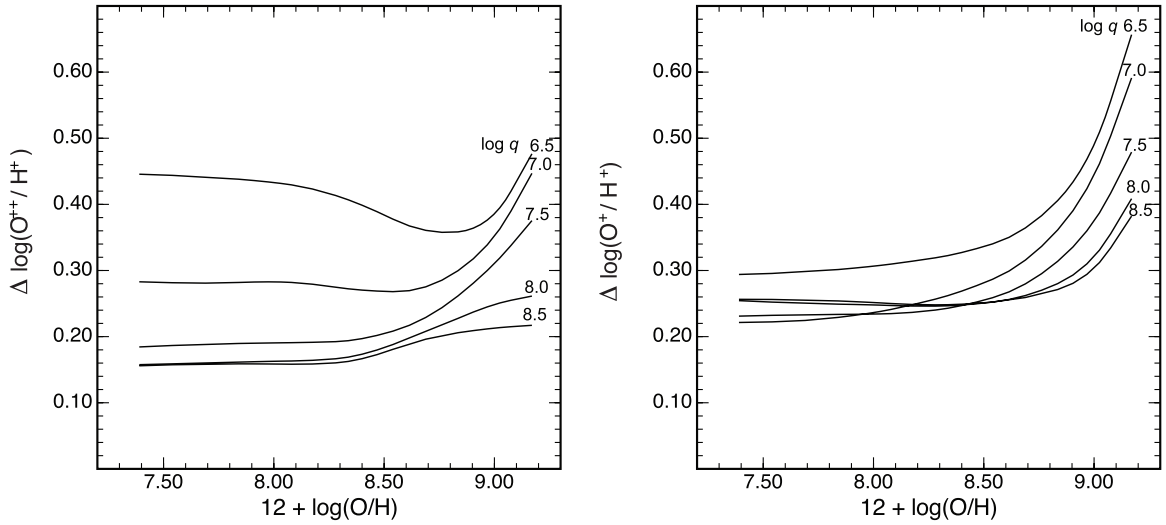

Figure 32. Offset in abundance implied between the strong line techniques and the T_e method for O^{++}/H^+ (left) and O^+/H^+ (right), for an assumed value of $\kappa = 20$. The x-axis is the true nebular abundance. The theoretical offset is close to the actual difference observed for H II regions (López-Sánchez et al. 2012), suggesting that κ-distributed electrons might be capable of resolving this long-standing abundance discrepancy problem.

The κ-distributed electrons affect the T_e method in two separate ways. First, as pointed out by Nicholls et al. (2012, 2013), the κ-distribution directly affects the electron temperature measured by the usual temperature-sensitive line ratios such as [O III] λ4363/[O III] λ5007. This effect is most marked at the high abundance end of the scale (low electron temperature end), as can be seen in Table 6. This effect dies away for abundances below about 0.3 solar (although errors caused by use of the older temperature-averaged collisional strengths persist down to much lower abundances; Nicholls et al. 2013). Since the inferred electron temperature is higher than the electron temperature for M–B distributed electrons, the effect is to systematically underestimate the true abundance with the T_e method.

The second factor is that, at the temperatures typical of H II regions, collisional excitation rates for strong lines such as [O III] λ5007 and [O II] λλ3727, 9 are reduced in a κ-distribution, while the strengths of the recombination lines are increased. This fact weakens these strong lines relative to the Balmer lines, leading to a further underestimate of the ionic abundances and adding to the systematic offset between strong-line techniques and the T_e method. The weakening of these forbidden lines with respect to the hydrogen recombination lines is more significant at the low end of the abundance scale, as can be clearly seen in Figures 9 and 19.

We have estimated the size of these two effects for $\kappa = 20$ using the ratio of the collisional excitation rates implied by the inferred electron temperatures given in Table 6 for $\kappa = 20$ and $\kappa = \infty$: the M–B case. This correction factor has to be further corrected by multiplying by the ratio of the forbidden line considered—in this case, [O III] λ5007 and [O II] λλ3727, 9 evaluated at $\kappa = \infty$ and $\kappa = 20$. In effect, we are assuming that the derived abundance scales as the chosen line ratio with respect to Hβ. The line strengths are drawn from Table 4.

The results of these computations are shown in Figure 32, which shows the estimated offset between the model-based strong-line method and the T_e method for the ionic ratios O^{++}/H^+ and O^+/H^+, which are fundamental for deriving O/H in the T_e method. Typical offsets lie between 0.2 and 0.4 dex, which are very similar to the observed offset—see (for example) López-Sánchez et al. (2012), Figue 12. We conclude that κ-distributed electrons may well provide the key to resolving the long-standing abundance discrepancy problem in H II regions.

9. CONCLUSIONS

In this paper, we have investigated the consequences of the assumption of κ-distributed electrons rather than M–B distributed electrons on strong-line abundance diagnostics. These models also account for the impact of new atomic data on collisional excitation rates and transition probabilities, and the effect of the revised solar abundance scale (Grevesse et al. 2010).

We have treated κ as a free variable in the grid of models presented here, so that observers can elect either to use or not to use κ. However, with $\kappa \sim 20$, or somewhat larger, the observed offset between the recombination temperature of bright H II regions and the electron temperatures inferred for both the high- and low-excitation zones can be explained.

With $\kappa \sim 20$, the UV lines of high-abundance, low electron temperature H II regions are predicted to be very strongly enhanced, whereas the effect of κ on the mid- and far-IR lines is weak, ranging from 2% to 25%. Our models clearly have some issues in their predictions of the intensities of some of the mid-IR lines, which is likely to be due to our choice of low density and zero age (Snijders et al. 2007).

For the strong lines at optical wavelengths, we have developed a new set of diagnostic diagrams that rely on the ratios of two forbidden lines rather than the ratio of a forbidden line to a recombination line of hydrogen, as has mostly been used hitherto. These new diagnostics cleanly separate the two parameters that principally determine the strong line emission spectrum: the chemical abundance set and the ionization parameter.

However, the derived abundance scale derived in this paper suffers from a weakness of relying on the ratio of [N II] to either of the α-process ions, [O II] or [S II]. Thus, this abundance scale is highly sensitive to how well the N/O versus O/H relation shown in Figure 3 can be calibrated. This relationship clearly has scatter, especially at the low abundance end, and the reasons for this scatter have been discussed by many authors (Matteucci & Tosi 1985; Henry et al. 2000; Contini et al. 2002; López-Sánchez & Esteban 2010)—see the recent summary by Pilyugin & Thuan (2011). For a given change in the N/O ratio at fixed

O/H, the calibrations involving the [N II]/[S II] ratio will be more affected than those that depend on the [N II]/I [O II] ratio, since the total range in the [N II]/[S II] ratio is more restricted than that of the [N II]/[O II] ratio. In addition, the ratio of the secondary nucleosynthetic production of nitrogen to the primary component is sensitive to the IMF, which may change between galaxies. Nonetheless, the fact that the derived abundance is monotonic with the abundance sensitive ratio used is a notable advantage compared to the use of the ratio of a forbidden line to a recombination line of hydrogen, which must always be a two-valued function of abundance. The latter ratios then have to be calibrated with an assumption of which solution branch applies, and furthermore there is a wide range of abundance over which the ratio of a forbidden line to a recombination line of hydrogen is insensitive to changes in the abundance.

The primary effect of the new atomic data and the self-consistency between the abundance set used in the stellar atmospheres and the abundance set used in the H II region models is to produce, for the first time, a fully consistent solution for the nebular abundances and the nebular ionization parameter between some half dozen strong-line diagnostics. This result greatly increases confidence in their use, as well as in the N/O versus O/H calibration used here.

$\kappa \sim 20$ assists in resolving the long-standing abundance discrepancy between the strong-line and T_e-based techniques of deriving the nebular abundance. At the high abundance end, κ increases the electron temperature measured from the ratio of two forbidden lines, which leads to the T_e method delivering too low abundances. At the low abundance end, the effect of κ is to decrease the forbidden lines relative to the recombination lines of hydrogen. This effect also will lead to the T_e method delivering too low abundances. These effects seem, in principle, to account for all of the abundance discrepancy between the strong-line and T_e + ICF-based techniques. This important point will be examined in greater detail in a future paper.

REFERENCES

Allen, M. G., Groves, B. A., Dopita, M. A., Sutherland, R. S., & Kewley, L. J. 2008, ApJS, 178, 20
Aller, L. H., & Liller, W. 1959, ApJ, 130, 45
Alloin, D., Collin-Souffrin, S., Joly, M., & Vigroux, L. 1979, A&A, 78, 200
Badnell, N. R., & Griffin, D. C. 2000, JPhB, 33, 4389
Baldwin, J. A., Phillips, M. M., & Terlevich, R. 1981, PASP, 93, 5
Beccari, G., Spezzi, L., De Marchi, G., et al. 2010, ApJ, 720, 1108
Bell, K. L., Berrington, K. A., & Thomas, M. R. J. 1998, MNRAS, 293, L83
Berrington, K. A., Burke, V. M., Burke, P. G., & Scialla, S. 1989, JPhB, 22, 665
Berrington, K. A., Burke, P. G., Dufton, P. L., & Kingston, A. E. 1985, ADNDT, 33, 195
Bhatia, A. K., & Landi, E. 2012, ADNDT, in press
Blum, R. D., & Pradhan, A. K. 1992, ApJS, 80, 425
Bothun, G. D., Romanishin, W., Strom, S. E., & Strom, K. M. 1984, AJ, 89, 1300
Bresolin, F., Garnett, D. R., & Kennicutt, R. C. 2004, ApJ, 615, 228
Burgess, A., & Tully, J. A. 1992, A&A, 254, 436
Contini, T., Treyer, M. A., Sullivan, M., & Ellis, R. S. 2002, MNRAS, 330, 75
De Lucia, G., Kauffmann, G., & White, S. D. M. 2004, MNRAS, 349, 1101
De Marchi, G., Paresce, F., Panagia, N., et al. 2011, ApJ, 739, 27
Dere, K. P., Landi, E., Mason, H. E., Monsignori Fossi, B. C., & Young, P. R. 1997, A&AS, 125, 149
Diaz, A. I., & Pérez-Montero, E. 2000, MNRAS, 312, 130
Dopita, M. A. 1997, ApJL, 485, L41
Dopita, M. A., Fischera, J., Sutherland, R. S., et al. 2006a, ApJ, 647, 244
Dopita, M. A., Fischera, J., Sutherland, R. S., et al. 2006b, ApJS, 167, 177
Dopita, M. A., Groves, B. A., Fischera, J., et al. 2005, ApJ, 619, 755
Dopita, M. A., Groves, B. A., Sutherland, R. S., Binette, L., & Cecil, G. 2002, ApJ, 572, 753
Dopita, M. A., Kewley, L. J., Heisler, C. A., & Sutherland, R. S. 2000, ApJ, 542, 224
Dopita, M. A., & Sutherland, R. S. 2000, ApJ, 539, 742
Edmunds, M. G., & Pagel, B. E. J. 1984, MNRAS, 211, 507
Esteban, C. 2002, RMxAC, 12, 56
Esteban, C., Bresolin, F., Peimbert, M., et al. 2009, ApJ, 700, 654
Esteban, C., Peimbert, M., García-Rojas, J., et al. 2004, MNRAS, 355, 229
Evans, I. N., & Dopita, M. A. 1985, ApJS, 58, 125
Evans, I. N., & Dopita, M. A. 1986, ApJ, 307, 431
Froese Fischer, C., Tachiev, G., Rubin, R. H., & Rodríguez, M. 2009, ApJ, 703, 500
Galavís, M. E., Mendoza, C., & Zeippen, C. J. 1995, A&AS, 111, 347
Galavís, M. E., Mendoza, C., & Zeippen, C. J. 1998, A&AS, 133, 245
García-Rojas, J., & Esteban, C. 2007, ApJ, 670, 457
García-Rojas, J., Esteban, C., Peimbert, A., et al. 2005a, MNRAS, 362, 301
García-Rojas, J., Esteban, C., Peimbert, M., et al. 2005b, ApJS, 153, 501
García-Rojas, J., Esteban, C., Peimbert, M., et al. 2006, MNRAS, 368, 253
Garnett, D. R., Dufour, R. J., Peimbert, M., et al. 1995a, ApJ, 449, 77
Garnett, D. R., Edmunds, M. G., Henry, R. B. C., Pagel, B. E. J., & Skillman, E. D. 2004, AJ, 128, 2772
Garnett, D. R., Shields, G. A., Peimbert, M., et al. 1998, ApJ, 513, 168
Garnett, D. R., Skillmann, E. D., Dufour, R. J., et al. 1995b, ApJ, 443, 64
Giveon, U., Sternberg, A., Lutz, D., Feuchtgruber, H., & Pauldrach, A. W. A. 2002, ApJ, 566, 880
Grevesse, N., Asplund, M., Sauval, A. J., & Scott, P. 2010, Ap&SS, 328, 179
Henry, R. B. C., Edmunds, M. G., & Köppen, J. 2000, ApJ, 541, 660
Hudson, C. E., Ramsbottom, C. A., & Scott, M. P. 2012, ApJ, 750, 65
Kauffmann, G., Heckman, T. M., Tremonti, C., et al. 2003, MNRAS, 346, 1055
Kewley, L. J., & Dopita, M. A. 2002, ApJS, 142, 35
Kewley, L. J., & Ellison, S. L. 2008, ApJ, 681, 1183
Kewley, L. J., Groves, B., Kauffmann, G., & Heckman, T. 2006, MNRAS, 372, 961
Kewley, L. J., Rupke, D., Zahid, H. J., Geller, M. J., & Barton, E. J. 2010, ApJ, 721, 48
Kimura, Mann, & Jessberger, 2003, ApJ, 582, 846
Kingdon, J. B., & Ferland, G. J. 1995, ApJ, 450, 691
Kobayashi, C., Springel, V., & White, S. D. M. 2007, MNRAS, 376, 1465
Kobulnicky, H. A., & Kewley, L. J. 2004, ApJ, 617, 240
Kramida, A., Ralchenko, Yu., & Reader, J. NIST ASD Team 2012, NIST Atomic Spectra Database (ver. 5.0), Accessed: http://physics.nist.gov/asd (2012 November 26)
Landi, E., & Bhatia, A. K. 2005, ADNDT, 89, 139
Landi, E., Del Zanna, G., Young, P. R., Dere, K. P., & Mason, H. E. 2012, ApJ, 744, 99
Leitherer, C., & Heckman, T. M. 1995, ApJS, 96, 9
Leitherer, C., Schaerer, D., Goldader, J. D., et al. 1999, ApJS, 123, 3
Lejeune, Th., Cuisinier, F., & Buser, R. 1997, A&AS, 125, 229
Liang, G. Y., & Badnell, N. R. 2011, A&A, 528, A69
Livadiotis, G., & McComas, D. J. 2011, ApJ, 741, 88
Livadiotis, G., McComas, D. J., Dayeh, M. A., Funsten, H. O., & Schwadron, N. A. 2011, ApJ, 734, 1
López-Sánchez, Á. R., Dopita, M. A., Kewley, L. J., Zahid, H. J., Nicholls, D. C., & Scharwächter, J. 2012, MNRAS, 426, 2630
López-Sánchez, Á. R., & Esteban, C. 2010, A&A, 517, A85
López-Sánchez, Á. R., Esteban, C., García-Rojas, J., Peimbert, M., & Rodríguez, M. 2007, ApJ, 656, 168
Mathis, J. S., Rumpl, W., & Nordsieck, K. H. 1977, ApJ, 217, 425 (MRN)
Matteucci, F., & Tosi, M. 1985, MNRAS, 217, 391
McGaugh, S. S. 1991, ApJ, 380, 140
Mendoza, C., & Zeippen, C. J. 1982, MNRAS, 199, 1025
Mohr, P. J., Taylor, B. N., & Newell, D. B. 2012, RvMP, 84, 1527
Nagamine, K., Fukugita, M., Cen, R., & Ostriker, J. P. 2001, ApJ, 558, 497
Nicholls, D. C., Dopita, M. A., & Sutherland, R. S. 2012, ApJ, 752, 148
Nicholls, D. C., Dopita, M. A., Sutherland, R. S., Kewley, L. J., & Palay, E. 2013, ApJS, 207, 21
Nussbaumer, H., & Storey, P. J. 1980, A&A, 89, 308
Nussbaumer, H., & Storey, P. J. 1988, A&A, 193, 327
Oey, M. S., Shields, J. C., Dopita, M. A., & Smith, R. C. 2002, RMxAC, 12, 77
Pagel, B. E. J., Edmunds, M. G., Blackwell, D. E., Chun, M. S., & Smith, G. 1979, MNRAS, 189, 95
Palay, E., Nahar, S. N., Pradhan, A. K., & Eissner, W. 2012, MNRAS, 423, 35
Peimbert, A. 2003, ApJ, 584, 735
Peimbert, M. 1967, ApJ, 150, 825
Peimbert, M., & Costero, R. 1969, BOTT, 5, 3
Peña-Guerrero, M. A., Peimbert, A., Peimbert, M., & Ruiz, M. T. 2012, ApJ, 746, 115
Pequignot, D., & Aldrovandi, S. M. V. 1976, A&A, 50, 141
Pettini, M., & Pagel, B. E. J. 2004, MNRAS, 348, 59

Pilyugin, L. S. 2001a, A&A, 369, 594
Pilyugin, L. S. 2001b, A&A, 374, 412
Pilyugin, L. S., Grebel, E. K., & Mattsson, L. 2012, MNRAS, 424, 2316
Pilyugin, L. S., & Mattsson, L. 2011, MNRAS, 412, 1145
Pilyugin, L. S., & Thuan, T. X. 2005, ApJ, 631, 231
Pilyugin, L. S., & Thuan, T. X. 2011, ApJL, 726, L23
Press, W. H., & Forbes, T. 2007, Numerical Recipes (3rd ed.; Cambridge: Cambridge Univ. Press)
Ramsbottom, C. A., Bell, K. L., & Keenan, F. P. 1998, MNRAS, 293, 233
Ramsbottom, C. A., Berrington, K. A., Hibbert, A., & Bell, K. L. 1994, PhyS, 50, 246
Rich, J. A., Torrey, P., Kewley, L. J., Dopita, M. A., & Rupke, D. S. N. 2012, ApJ, 753, 5
Rupke, D. S. N., Kewley, L. J., & Chien, L.-H. 2010, ApJ, 723, 1255
Schmutz, W., Leitherer, C., & Gruenwald, R. B. 1992, PASP, 104, 1164
Skillman, E. D., Kennicutt, R. C., & Hodge, P. W. 1989, ApJ, 347, 875
Snijders, L., Kewley, L. J., & van der Werf, P. P. 2007, ApJ, 669, 269
Stafford, R. P., Bell, K. L., & Hibbert, A. 1994, MNRAS, 266, 715
Stasińska, G. 2004, in Cosmochemistry: The Melting Pot of the Elements, ed. C. Esteban, R. J. García López, A. Herrero, & F. Sánchez (Cambridge: Cambridge Univ. Press), 115
Stasińska, G. 2006, A&A, 454, L127
Stasińska, G., Cid Fernandes, R., Mateus, A., Sodré, L., & Asari, N. V. 2006, MNRAS, 371, 972
Sutherland, R. S., & Dopita, M. A. 1993, ApJS, 88, 253
Tachiev, G., & Froese Fischer, C. 1999, JPhB, 32, 5805
Tachiev, G., & Froese Fischer, C. 2000, JPhB, 33, 2419
Tachiev, G., & Froese Fischer, C. 2001, CaJPh, 79, 955
Tachiev, G., & Froese Fischer, C. 2002, A&A, 385, 716
Tayal, S. S. 2000, ADNDT, 76, 191
Tayal, S. S. 2006, ApJS, 163, 207
Tayal, S. S. 2007, ApJS, 171, 331
Tayal, S. S. 2008, A&A, 486, 629
Tayal, S. S. 2011, ApJS, 195, 12
Tayal, S. S., & Zatsarinny, O. 2010, ApJS, 188, 32
Torrey, P., Cox, T. J., Kewley, L., & Hernquist, L. 2012, ApJ, 746, 108
van Zee, L., Salzer, J. J., Haynes, M. P., O'Donoghue, A. A., & Balonek, T. J. 1998, AJ, 116, 2805
Veilleux, S., & Osterbrock, D. E. 1987, ApJS, 63, 295
Vila-Costas, M. B., & Edmunds, M. G. 1992, MNRAS, 259, 121
Wyse, R. F. G., & Silk, J. 1985, ApJL, 296, L1
Yuan, T.-T., Kewley, L. J., & Richard, J. 2013, ApJ, 763, 9
Zaritsky, D., Kennicutt, R. C., & Huchra, J. P. 1994, ApJ, 420, 87
Zatsarinny, O., & Tayal, S. S. 2003, ApJS, 148, 575